processes

Article

Solidification Treatment of Wastewater and Waste Soil Generated during Binhai Reclamation: A Study on Mechanical Properties and Resource Utilization

Aiwu Yang [1,*], Jian Xu [1] and Caili Xu [2]

[1] College of Environmental Science and Engineering, Donghua University, Shanghai 201620, China; jianxuchn@163.com
[2] Key Laboratory of Soft Soil Characteristics and Engineering Environment of Tianjin, Tianjin Chengjian University, Tianjin 300384, China
* Correspondence: tulilab@163.com

Abstract: Coastal reclamation projects generate an accumulation of wastewater and waste soil, resulting in highly saturated soft soil. Presently, there is a scarcity of research regarding the lightweight solidification and three-dimensional mechanical properties of these soils. Additionally, there is a dearth of specialized models for stabilizing soils containing wastewater using lightweight solidification technology, and pertinent engineering solutions are lacking. By introducing solidifying agents and foaming agents to treat wastewater in soft fill soil, a novel type of solidified lightweight material is produced, imparting strength. This study investigates its three-dimensional mechanical properties. During triaxial tests with equal stress (σ3) and equal b values, the softening of the curve noticeably diminished at b = 0.25. In the plane strain test, cohesion increased by 10.7% compared to the traditional triaxial tests, and the internal friction angle increased by 11%. Subsequently, a three-dimensional Cambridge model was established. At elevated confining pressures, the corrected curve closely approximated the test curve, demonstrating a minimum model accuracy of approximately 96% at a confining pressure of 20 KPa. These findings offer valuable numerical references and a theoretical foundation for the efficient utilization of wastewater and waste soil.

Keywords: wastewater; solidified lightweight soil; physio-chemical processes; sustainable utilization; mechanical properties

check for updates

Citation: Yang, A.; Xu, J.; Xu, C. Solidification Treatment of Wastewater and Waste Soil Generated during Binhai Reclamation: A Study on Mechanical Properties and Resource Utilization. *Processes* **2023**, *11*, 2983. https://doi.org/10.3390/pr11102983

Academic Editors: Carlos Sierra Fernández and Antoni Sanchez

Received: 20 September 2023
Revised: 8 October 2023
Accepted: 11 October 2023
Published: 15 October 2023

1. Introduction

The rapid pace of urbanization has created a critical shortage of available land for urban construction, compelling many coastal cities to initiate projects for reclaiming land along their coastlines. These initiatives not only relieve the pressure on urban land usage but also promote vigorous and dynamic growth within the urban economy. For instance, the ongoing and extensive coastal reclamation project in the Binhai New Area of Tianjin provides a relevant example. However, these reclamation projects inevitably lead to the production of considerable quantities of waste soil and sewage. The combination of these waste materials creates a mixture characterized by high water content, low strength, notable compressibility, and restricted permeability, making it unsuitable for practical engineering purposes. At the same time, the substantial accumulation of sewage and waste soil leads to the diminishment of land resources and severe environmental pollution. Consequently, it is imperative to innovate with solidification materials for the treatment of wastewater and waste soil, addressing the vulnerabilities related to low strength, high water content, and structural instability within the waste soil–wastewater amalgam. In practical engineering scenarios, solidified soil experiences diverse loads, including fill soil and dynamic forces, resulting in an intricate three-dimensional stress condition. Traditional testing equipment encounters challenges in accurately and comprehensively replicating these loading conditions. Furthermore, the mechanical attributes of the soil exhibit significant complexity owing to various influencing factors, and simplistic elastoplastic models fail to provide an accurate depiction of its genuine stress state and mechanical traits. Consequently, there is a need for the ongoing enhancement of solidification techniques, resolution of the engineering challenges inherent in high-water-content fill locations, and extensive investigation into the associated mechanical evolution mechanisms. This endeavor bears substantial economic and social significance in facilitating the rational and effective utilization of high-water-content fill soil while expediting engineering construction.

Both domestic and international scholars have made significant progress in researching the solidification treatment of reclaimed land resulting from the accumulation of wastewater and waste soil. They have also investigated the three-dimensional stress–strain relationship of solidified soil and explored elastoplastic constitutive models. Shen et al. [1] utilized slag as the primary constituent, complemented by activators like water glass and gypsum powder, to solidify and remediate hydraulic fill with a high water content. Yang et al. [2] conducted an investigation into the correlation between the dosage of fly ash, a key constituent of solid waste-based solidifying agents, and the levels of cohesion and internal friction angle. They delved into the linear relationship between these factors. Additionally, they examined the connection between the pore structure of the solidified soil and the hydration products that ensued from the process [3]. Lei et al. [4] employed anionic polyacrylamide to treat solidified soil. Li et al. [5] conducted an innovative investigation on soft soil stabilization in hydraulic fill using microbial-induced calcium carbonate precipitation. Soganci et al. [6] utilized slag as a solidifying agent for soft clay and investigated the solidification effect when combined with marble dust. Jia et al. [7] employed solid waste materials including steel slag and desulfurization ash in a cooperative solidification procedure to treat high-water-content soil. The optimum solidifying agent formulation was achieved with steel slag constituting seventy percent. Cui et al. [8] investigated the enhancement of performance of high-water-content dredged slurry utilizing steel slag. Shi et al. [9] collaborated on the use of steel slag and cement to mitigate the challenge posed by a high water content in dredged soft soil. Huang et al. [10] developed a comprehensive understanding of the adverse mechanical effects concerning the moisture content and the ratio of intermediate principal stress through rigorous true triaxial testing. However, as this ratio and moisture content increased, the detrimental effect gradually became more pronounced. Rong et al. [11] collaborated on a study investigating the mechanical properties of clay in frozen states within mining areas, employing orthogonal experiments and true triaxial tests. The results suggest that various factors, including temperature, moisture content, and confining pressure, significantly influence strength indicators. Zheng et al. [12] enhanced the fundamental true triaxial apparatus by implementing multiple partitions to mitigate interference during loading. The apparatus underwent testing through a series of one hundred experiments, providing insights into the failure mode of loess. In their research, Gu et al. [13] analyzed the coupling of different stresses, investigating scenarios where both compression and tension states coexist and lead to separation at a certain threshold. Zheng et al. [14] carried out numerous isotropic consolidation tests on loess with the aim of exploring the failure envelope and mechanical properties of this material. Han et al. [15] investigated the contact density and liquefaction properties of geomaterials at a critical state. Li et al. [16] integrated the GDS apparatus with a true triaxial setup, revealing a critical point in the failure behavior of aeolian sand. Shao et al. [17] employed a true triaxial apparatus to investigate the failure modes of shear bands under low confining pressure. Additionally, they modified the intermediate principal stress to establish a model. Zhang et al. [18] developed anisotropic boundary conditions for the analysis of dams and subsequently compared them with conventional constitutive models. Cabrejos et al. [19] conducted true triaxial tests, considering intricate factors like particle size distribution, to derive suitable models. Salimi et al. [20] incorporated fluid coupling in their true triaxial experiments to investigate the mechanical characteristics of simulated soil particles. Ren et al. [21] explored the impact of temperature factors on true triaxial tests and investigated the corresponding degradation conditions. Cao et al. [22] studied the variation trend of deformation of high-calcium clay, considering the combined influence of various factors, including the salt content and temperature. Shao et al. [23] conducted true triaxial experiments, taking into account the influence of matric suction factors, and subsequently analyzed the geostress. Shao et al. [24] modified the true triaxial apparatus by incorporating a balance plate and a hydraulic chamber. They also designed algorithms for research. Andreghetto et al. [25] incorporated a true triaxial apparatus into an automated program and verified its functionality by comparing it with conventional experimental instruments. Sun et al. [26] performed a collaborative analysis of load tests utilizing true triaxial experiments and fractional plasticity models. Foroutan et al. [27] developed a model that correlates confining pressure with porosity, investigating the significant influence of the intermediate principal stress ratio. Liu et al. [28] developed a model that correlates confining pressure with porosity, investigating the significant influence of the intermediate principal stress ratio. Huang et al. [29] employed a modified apparatus to investigate frozen soil under complex stress conditions. Shao et al. [30] explored the strength variation of soil following natural structural failure and investigated the impact of microcracks on the strength pattern through the use of true triaxial tests. Liu et al. [31] formulated a three-dimensional creep model and then optimized it specifically for accelerated creep conditions. Wang et al. [32] refined an elastoplastic constitutive model to account for non-uniform deformation and fracture, enhancing its applicability in capturing the dynamic characteristics of soil. Yamada et al. [33] introduced a novel approach to integrate cementation into the current elastoplastic constitutive model of soil. Zheng et al. [34] introduced velocity parameters into the prediction model. This model demonstrated enhanced predictive performance, particularly for extended creep durations. Tachibana et al. [35] incorporated parameters related to the compaction curve into the constitutive model, resulting in simulation results of higher accuracy. Zhao et al. [36] conducted triaxial tests on soft soil, considering the coupling conditions of cyclic loading and the salt content. Zhang et al. [37] formulated a binary medium computational model for samples, treating them as two-phase materials. They proceeded to validate and calibrate the model. Peng et al. [38] formulated a constitutive model with the ability to accurately predict uncertain boundary values. Subsequently, they conducted validation to assess its performance. Mazzucco et al. [39] examined the peak strength of nonlinear materials employing a model loaded via a novel procedure. Sternik et al. [40] studied a constitutive model that integrated temperature and hardening parameters. They then compared experimental data with the predicted results across diverse loading conditions. In summary, enhancing soil engineering properties through the addition of solidifying materials is well acknowledged in both academic and engineering circles. The preceding research has established a robust foundation for more effective soil treatment. However, there has been insufficient research on soft soil reclamation with a high moisture content, especially in coastal areas, in the studies mentioned. Various materials are available for soil management, each differing in composition and properties, primarily emphasizing the strength of the solidified soil after the interaction between solidifying agents and the soil. However, research on the influence of factors like moisture content and foaming rate on the strength of the solidified soil is notably scarce in the studies mentioned. Hence, the development of stabilization technology for coastal, highly saturated reclaimed soils that simultaneously enhances the soil strength while reducing the bulk density is of significant engineering and academic value. In reviewing the research and experimental findings on diverse types of soil conducted by a multitude of scholars employing various methodologies globally and domestically, it becomes evident that true triaxial tests yield results that better depict the stress–strain characteristics of soils in practical engineering when contrasted with simplistic direct shear or unconfined compression strength tests. Until now, research on the three-dimensional mechanical properties of solidified lightweight soil has been limited. Hence, investigating the stress–strain characteristics of solidified lightweight soil under actual three-dimensional stress conditions holds paramount scientific and practical importance. Presently, scholars, both nationally and internationally, have conducted research to varying extents concerning the formulation of constitutive models for rock and soil materials, yielding relevant outcomes. Nonetheless, research regarding the constitutive model of solidified lightweight soil, a novel subgrade material, remains limited. Aligning with the national sustainable development strategy, the integration of novel geotechnical materials into subgrade construction represents a prevailing trend. Hence, given the stress attributes of subgrade fill materials, developing the three-dimensional Cambridge model for solidified lightweight soil carries noteworthy theoretical and practical importance within the realm of engineering.

In this study, we utilize solidification technology to address the suboptimal mechanical properties of soft and viscous clay in the Tianjin Binhai reclamation area. Our objective is to ensure that the solidified lightweight soil, after undergoing this treatment, meets the requisite strength standards for engineering applications. Furthermore, this study furnishes theoretical underpinnings for ensuring the safe operation of the site. Subsequently, in light of the actual stress characteristics and engineering challenges present at the reclamation site, we conducted a thorough analysis of the three-dimensional mechanical properties of solidified lightweight soil under diverse stress pathways. This involved a comprehensive investigation into the three-dimensional mechanical constitutive model of solidified lightweight soil operating under the conditions of three-dimensional stress. The insights derived from this research offer both theoretical and technical support for the efficient and secure utilization of solidified lightweight soil in engineering applications.

2. Sample Preparation and Experimental Procedure

A diagram of the experimental research procedure of this paper is shown in Figure 1.

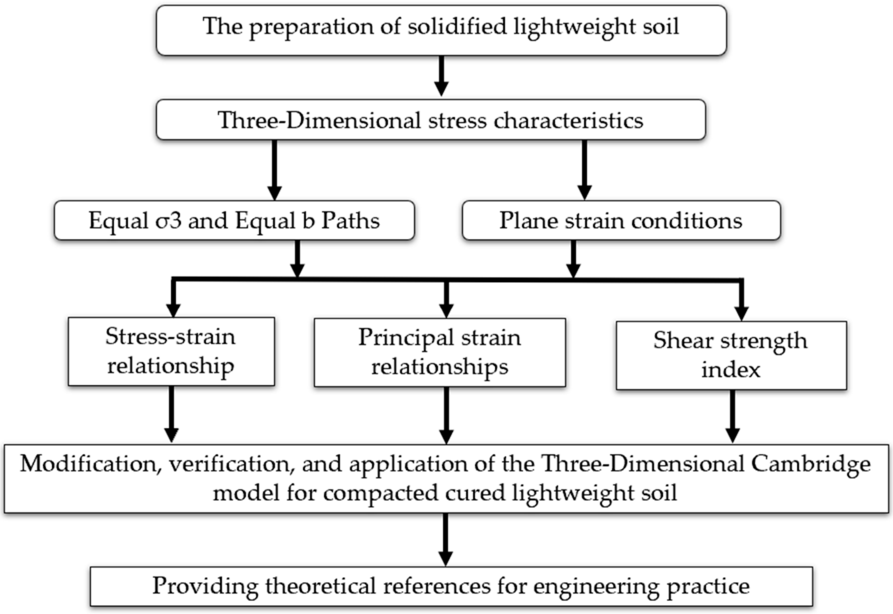

Figure 1. Experimental research program block diagram.

2.1. Experimental Material

This experimental study utilized clay with a high water content sourced from a recent reclamation site in Binhai New Area, Tianjin, China, as the foundational soil material. The soil is a blend of wastewater and waste soil accumulated post-reclamation, making it unsuitable for direct use as construction soil in nearby sites. Thus, it served as the focal soil for this investigation. Moreover, the sampled soil exhibits a notably high moisture content. Initially, the collected reclaimed soft soil was placed in an open, sunlit area. To facilitate more uniform and rapid drying, the highly adhesive soft soil was sectioned using a geotechnical knife. After approximately a week, the dried soil was thoroughly ground using a ball mill. The ground soil was then sifted through a 1 mm sieve to ensure uniformity, preparing it for subsequent experiments. The initial physical and mechanical properties of the original soil were assessed through laboratory experiments, and the results are presented in Table 1. In Table 1, the variables are defined as follows: ω for water content, ρ for density, e for void ratio, Gs for specific gravity, ω_L for liquid limit, ω_P for plastic limit, Ip for plasticity index, and I_L for liquidity index.

Table 1. Soil-related indicators of Tianjin Binhai reclamation fill.

ω/%	ρ/(g/cm^3)	e	Gs	ω_L/%	ω_P/%	I_p	I_L
47.8	1.75	1.287	2.74	43.4	25.1	18.5	1.19

For the stabilization of lightweight soil, a proprietary stabilizer was developed and employed, as indicated by the patent application number CN201610137156.3. This stabilizer comprises a primary and an auxiliary stabilizing agent. The primary constituent of this stabilizer is ordinary Portland cement, a prevalent silicate cement. The auxiliary element of the stabilizer is hydrated lime, chemically denoted as calcium oxide (CaO). This study utilized an experimental approach employing an orthogonal array design. During the formulation of lightweight soil mixtures for curing, four main factors were considered: I (moisture content), J (primary curing agent), K (auxiliary curing agent), and L (foaming agent). Each of these factors was investigated at four different levels. An orthogonal experimental design, represented by a 4 × 4 factorial matrix, was applied, as depicted in Table 2 below. The comprehensive results and analysis of the experiments are detailed in Table 3.

Table 2. Orthogonal test factor levels.

Horizontal Numbering	Factor			
	I Moisture Content	J Main Agent	K Auxiliary	L Foaming Agent
1	80%	5%	2%	0.06%
2	90%	7%	3%	0.07%
3	100%	9%	4%	0.08%
4	110%	11%	5%	0.09%

Note: The masses of the primary curing agent, auxiliary curing agent, and foaming agent were added based on the percentage of the total mass of water and dry soil.

Table 3. Analysis of orthogonal test results.

Analysis	7 Days				28 Days			
	I	J	K	L	I	J	K	L
T_1	296.76	48.46	79.19	119.17	727.62	150.46	281.56	330.55
T_2	171.03	87.97	97.94	168.59	419.53	287.51	313.57	374.9
T_3	79.40	200.69	214.99	153.0	252.25	560.3	484.66	433.45
T_4	74.14	284.21	229.21	180.57	230.53	631.66	550.14	491.03
A 1	74.19	12.12	19.80	29.79	181.91	37.62	70.39	82.64
A 2	42.76	21.99	24.49	42.15	104.88	71.88	78.39	93.73
A 3	19.85	50.17	53.75	38.25	63.06	140.08	121.17	108.36
A 4	18.54	71.05	57.30	45.14	57.63	157.92	137.54	122.76
Extremely poor	55.65	58.93	37.50	15.35	124.28	120.30	67.15	40.12
Better solution	A1	B4	C4	D4	A1	B4	C4	D4

In this context, the Ti value represents the sum of the unconfined compressive strength of each factor at the same i level, and the mean Ai value is calculated by dividing Ti by the number of factors. The optimal composition yielding the highest unconfined compressive strength for both the 7-day and 28-day periods in cured lightweight soil is clearly illustrated in Table 3, denoted as I1J4K4L4. It is notable that this composition consistently produced the highest strength throughout the testing period. Furthermore, an analysis of the table reveals that factor J demonstrated the highest variability in the 7-day results, followed by factor I. Similarly, in the 28-day results, factor I exhibited the highest variability, succeeded by factor J. This analysis suggests that the primary curing agent and moisture content exert a more substantial influence on the strength of cured lightweight soil compared to the auxiliary curing agent and foaming agent. The strength of cured lightweight soil primarily emanates from the hydration reactions between the curing agents and water, leading to binding and solidification. However, in practical engineering applications, prioritizing higher strength in cured lightweight soil is not the sole concern. A comprehensive approach considering various factors, including material cost and specific engineering requirements, is imperative. Additionally, this study considers the impact of foaming to optimize outcomes concerning both lightweight properties and strength. The results of the cured lightweight soil in row T3 closely align with those in row T4 for both the 7-day and 28-day tests, meeting the stipulated strength criteria. Therefore, considering both the strength and economic aspects, the chosen composition for optimal results was I1J3K3L3. Subsequent experiments were conducted based on this formulation.

The sampled clay was subjected to processes such as drying, grinding, and sieving (1 mm) before sample preparation. The mixture was proportioned based on the principles of orthogonal experiments. The final selected proportions consisted of 9% of the primary curing agent, 80% distilled water, 0.08% foaming agent, and 4% auxiliary curing agent. Under these optimal conditions, the density of the cured lightweight soil was 1.34 g/cm^3. After mixing the components, the mixture was placed in a container and thoroughly stirred. The mixture was then steadily poured into prepared molds (75 mm × 75 mm × 165 mm). Vibration was applied continuously during the layering process, with each layer vibrated for no less than 1 min. Once filled, the soil samples were wrapped with breathable impermeable fabric and secured with adhesive tape. After 36 h, the samples were demolded and sealed in plastic wrap.

2.2. Experimental Procedures

The experiments utilized the GCTS SPAX-2000 true triaxial testing apparatus. The apparatus primarily comprises a pressure chamber, a digital force-volume computer servo controller, and a data acquisition system. It is equipped with an autonomous servo loading system, allowing for independent control of the major, intermediate, and minor principal stresses. This setup enables stress–strain measurements under both static and dynamic conditions, simulating the genuine stress state of the soil.

During the mechanical property experiments of lightweight soil solidified by blow-filling along the σ3 and b paths, prior to commencing the test, it is imperative to fill the pressure chamber with water to establish the requisite confining pressure for the experiment. Initially, the triaxial compression of the sample is maintained at a consistent level. Subsequently, during the experiment, the confining pressure remains constant, and both the major principal stress σ1 and intermediate principal stress σ2 are incrementally raised while holding the value of b constant. Specific confining pressures (20–80 kPa) and intermediate principal stress ratios (0–1) were selected. Four different densities of compacted lightweight soil were prepared, denoted as 1.0ρ0, 1.1ρ0, 1.2ρ0, and 1.3ρ0. The undrained, unconsolidated shear test method was employed for the experiments, and the specific experimental plan is outlined in Table 4. In this context, σ3 represents the confining pressure, b signifies the ratio of the intermediate principal stress to the increment of the major principal stress, and ρ0 denotes the density of the compacted cured lightweight soil prepared based on the mixing ratio scheme after a curing period of 28 days. The notation 1.1ρ0 signifies 1.1 times the density ρ0, and this convention can be extended to other values.

Table 4. True triaxial test plan.

σ3 (kPa)	b	ρ (g/cm^3)
20	0/0.25/0.5/0.75/1	1.0ρ0, 1.1ρ0, 1.2ρ0, 1.3ρ0
40		
60		
80		

In the experimental investigation of the mechanical properties of compacted cured lightweight soil under the conditions of plane strain, this stress state was defined by the condition where the cross-sectional size and shape of the soil remain constant along the axis length after experiencing external forces. In this state, the three-dimensional stresses were unequal, while the strain in the direction of intermediate principal strain remained at zero. The experimental setup for the confining pressure remained consistent with that of the equal σ3 and equal b tests, employing specific values of 20–80 kPa. Additionally, the mechanical characteristics of the cured lightweight soil were studied at a specific confining pressure, varying the densities denoted as 1.0ρ0, 1.1ρ0, 1.2ρ0, and 1.3ρ0. Conventional triaxial shear tests were initially conducted to analyze and investigate the stress–strain relationship of the cured lightweight soil. These tests supplied crucial data for subsequent true triaxial tests. The undrained and unconsolidated (UU) shear test method was employed for the triaxial shear tests on specimens that had undergone a 28-day curing period. Detailed specifics of the experimental plan can be found in Table 5.

Table 5. The conventional triaxial shear test plan.

Shear Mode	Confining Pressure
Undrained, unconsolidated (UU)	20 Kpa, 40 KPa, 60 Kpa, 80 Kpa

3. Results and Discussion

3.1. Study of Three-Dimensional Mechanical Characteristics under Equal σ3 and Equal b Paths

3.1.1. (σ1–σ3)~ε1 Relationship Curves

Figure 2, presented below, depicts the stress–strain curves of the compacted and cured lightweight soil under various b parameter stress conditions, encompassing confining pressures of 20–80 kPa. In this context, σ1 denotes the major principal stress, ε1 denotes the major principal strain, ε2 represents the intermediate principal strain, and ε3 signifies the minor principal strain.

Observation of Figure 2 reveals similar patterns in the (σ1–σ3) ~ε1 curves under varying confining pressures. At identical confining pressures, prior to reaching the yield strength, the deviatoric stress demonstrated a linear increase as the axial strain increased. Throughout this stage, the soil maintained its structural integrity and ability to resist external pressure, primarily displaying elastic deformation. With the ongoing increase in the axial strain, the curve's slope gradually diminishes, initially decreasing and eventually stabilizing. This signifies that subsequent to reaching the yield strength, the rate of deviatoric stress escalation diminished. Under consistent confining pressure, an increase in the "b" value resulted in a gradual elevation of the slope of the curve, indicating a rise in the initial tangent modulus. Simply put, for a constant confining pressure, higher b values resulted in reduced soil deformation and a more prominent strain-hardening behavior. Specifically, when b = 0, the curve significantly differs from curves associated with other b values, showcasing a notable strain-softening phenomenon. As the b value increased, the soil's tendency to soften gradually diminished. Moreover, with a further increase in the b value, the intermediate principal stress σ2 rose, resulting in heightened lateral confinement of the soil and subsequently limiting its lateral deformation. This bolstered the soil's overall strength, evident in the diminished softening phenomenon at b = 0.25 compared to b = 0. Beyond b = 0.25, the curves exhibited a gradual increase in the axial strain between

1.1% and 1.3% and transformed into smoother curves. This phenomenon arose from the amplified lateral confinement of the soil at higher b values, enhancing the soil strength and diminishing the softening tendency, thus showcasing a strain-hardening trend.

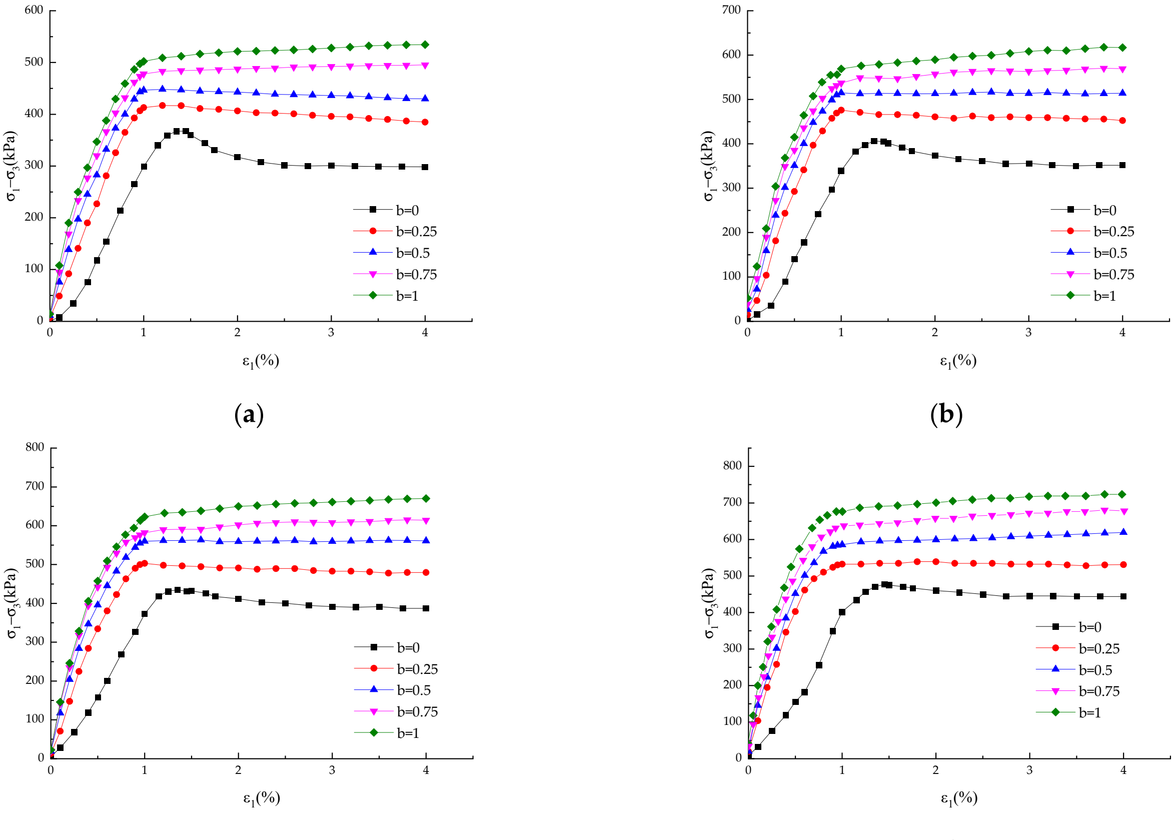

(**a**) (**b**)

(**c**) (**d**)

Figure 2. (σ1−σ3)~ε1 relationship curves under different confining pressure conditions: (**a**) 20 kPa; (**b**) 40 kPa; (**c**) 60 kPa; (**d**) 80 kPa.

Figure 3 depicts the relationship lines of the compacted lightweight soil under varying confining pressures while maintaining a constant intermediate principal stress ratio (b) of 0.5. The study encompasses densities ρ = 1.0ρ0, ρ = 1.1ρ0, ρ = 1.2ρ0, and ρ = 1.3ρ0.

As shown in Figure 3, when both the b value and ρ value were held constant, the deviatoric stress gradually increased with increasing confining pressure. Consequently, this yielded steeper curves, signifying an augmentation in the initial shear modulus. This observation implies that, for an equivalent strain level, the soil exposed to higher confining pressures necessitated more stress than the soil under lower confining pressures. The analysis indicates that increasing the confining pressure led to soil compaction, enhancing the interlocking capacity among the soil particles and intensifying their contact. Consequently, this resulted in heightened cohesion and augmented shear strength. Overall, the soil structure attained enhanced stability, demanding more energy to trigger failure.

Figure 4 illustrates the stress–deformation curves of the compacted lightweight soil under a 40 kPa confining pressure while maintaining a constant intermediate principal stress ratio (b) of 0.5. These curves correspond to four distinct densities: 1.0ρ0, 1.1ρ0, 1.2ρ0, and 1.3ρ0, as depicted in the figure.

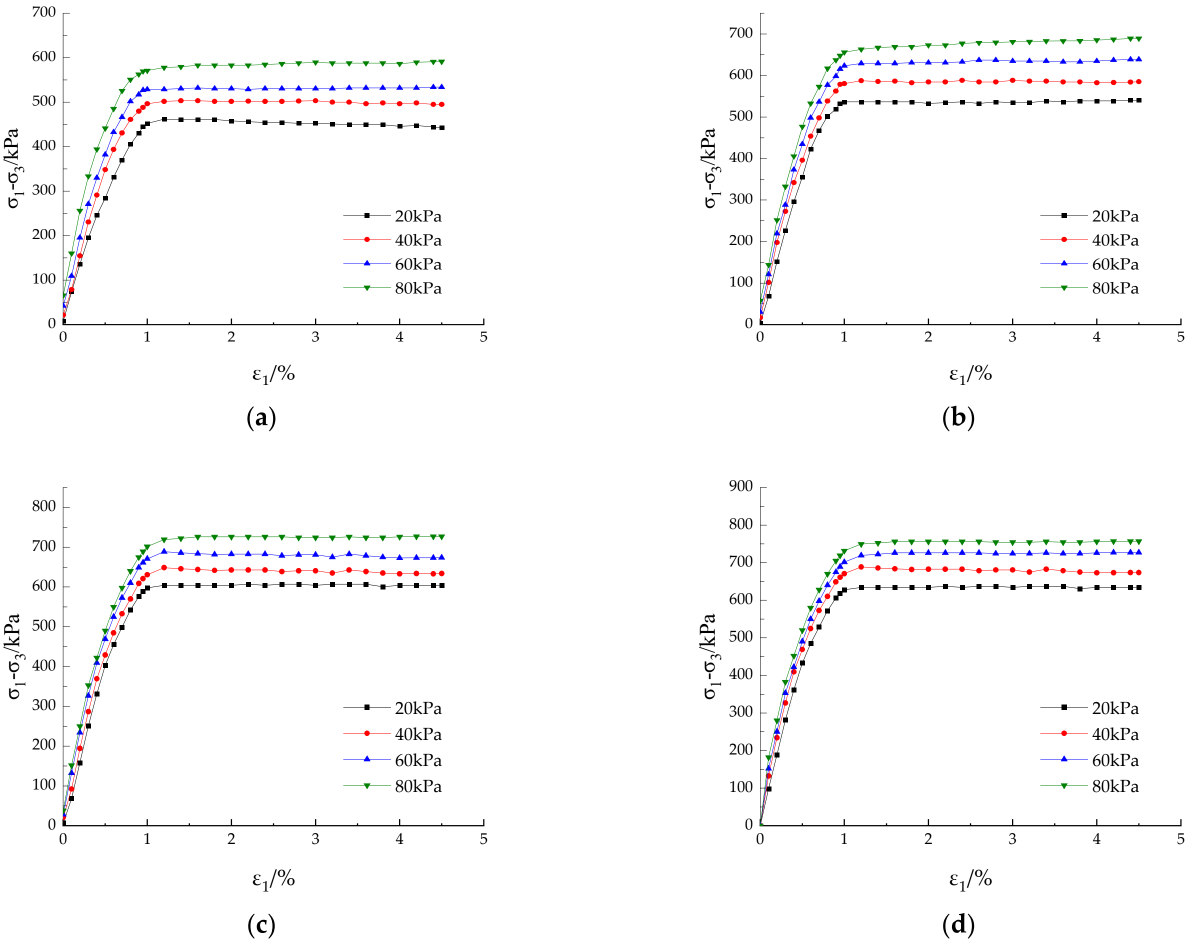

(**a**) (**b**)

(**c**) (**d**)

Figure 3. (σ1-σ3)~ε1 relationship curves under different density conditions: (**a**) ρ = 1.0ρ0; (**b**) ρ = 1.1ρ0; (**c**) ρ = 1.2ρ0; (**d**) ρ = 1.3ρ0.

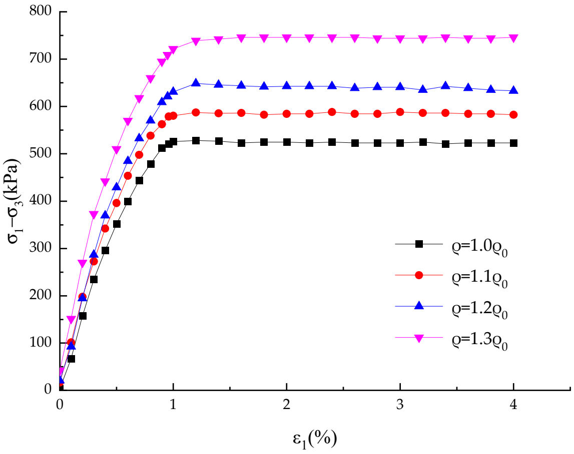

Figure 4. Stress–strain relationship curves at different densities.

Figure 4 clearly shows that under a 40 kPa confining pressure and with an intermediate principal stress ratio (b) of 0.5, the peak strength of the compacted and cured lightweight soil directly correlated with the density. Moreover, as the density increased, the peak strength curve shifted towards the right. In particular, the yield strain for ρ = 1.0ρ0 was 1.1%, and for ρ = 1.3ρ0, it increased to 1.3%. The underlying principle is as follows: A lower density corresponds to a reduced internal particle content within the soil, resulting in weaker bonding forces among the soil particles. As a consequence, when under loading, the soil's internal structure inadequately withstands pressure, causing a swift reach of the yield strength and subsequent structural failure. Conversely, with an increase in density, the soil comprises a higher number of particles with strengthened inter-particle bonding. This augmentation improves the soil's capacity to withstand external pressure, leading to a heightened yield strength and enhanced overall structural stability. Consequently, the high-density cured lightweight soil demonstrates elevated values for both the yield points and peak strength when juxtaposed with the low-density cured lightweight soil.

3.1.2. ε2~ε1 Relationship Curves

The relationship curves between ε2 and ε1 for the compacted and cured lightweight soil under varying confining pressures and densities were systematically investigated and analyzed. This study aimed to elucidate the interrelationships among distinct principal strains in compacted and cured lightweight soil. In this framework, compressive strain is regarded as the positive direction, while tensile strain is deemed the negative direction, as depicted in Figure 5.

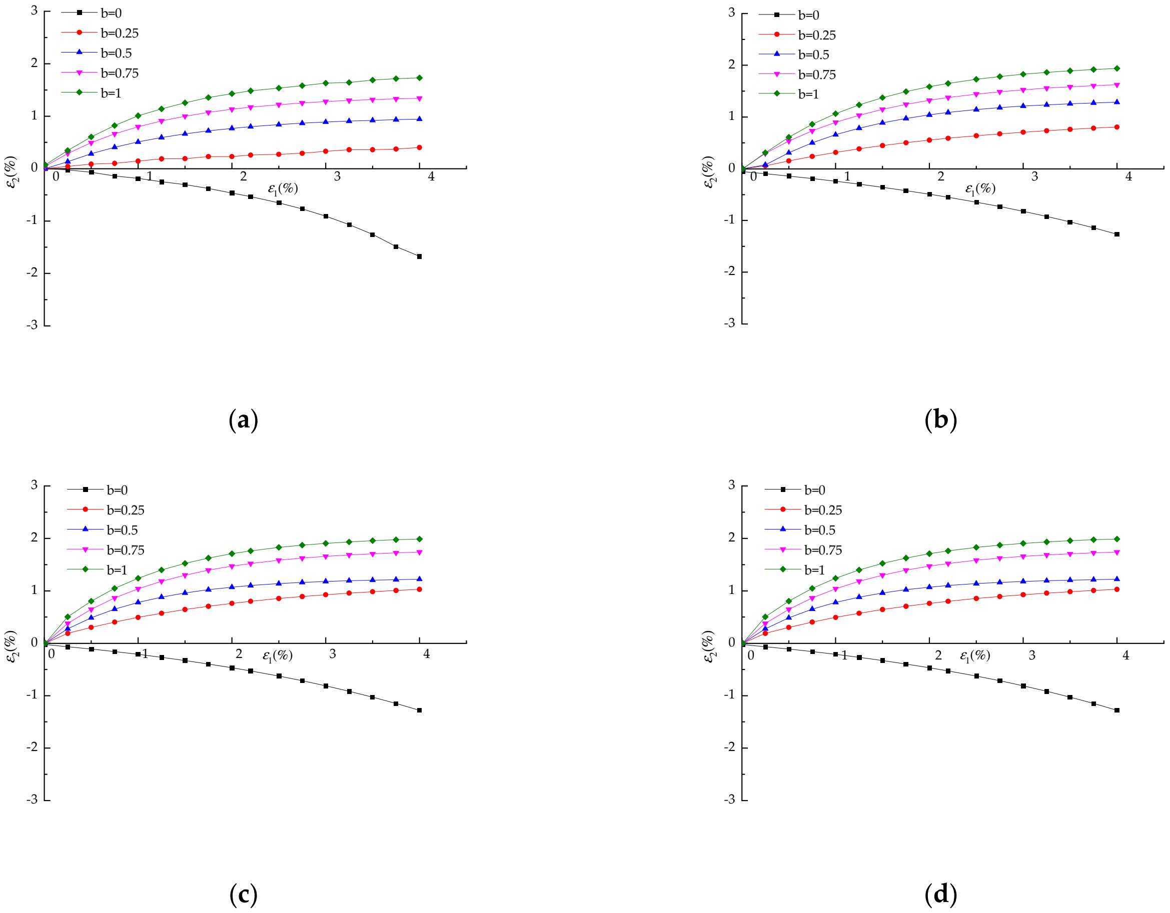

(**a**) (**b**)

(**c**) (**d**)

Figure 5. ε_2~ε_1 relationship curves under different confining pressure conditions: (**a**) 20 kPa; (**b**) 40 kPa; (**c**) 60 kPa; (**d**) 80 kPa.

Figure 5 demonstrates that under identical confining pressure conditions, the intermediate principal strain ε2 varied in direction with the changing b values. As the b value increased, ε2 exhibited an increase, and its direction shifted from expansion to compression. At b = 0, ε2 was negative, signifying soil expansion in this direction. At b = 0.25, the curve resides above the coordinate axis, indicating a positive ε2 value and showcasing a transition from expansion to compression in the intermediate principal strain direction for the soil. Thus, b = 0.25 can be identified as the critical value marking the shift in the deformation mode of the cured lightweight soil. Moreover, as the b value increased, the absolute value of the strain curve slope likewise increased. Put differently, with a larger b value, the intermediate principal strain was amplified for the same axial strain. Consequently, the b value exerted a substantial influence on the intermediate principal strain of the cured lightweight soil.

3.1.3. ε3~ε1 Relationship Curves

Figure 6 depicts the ε3~ε1 relationship curves of the cured lightweight soil under varying confining pressures: 20 kPa, 40 kPa, 60 kPa, and 80 kPa.

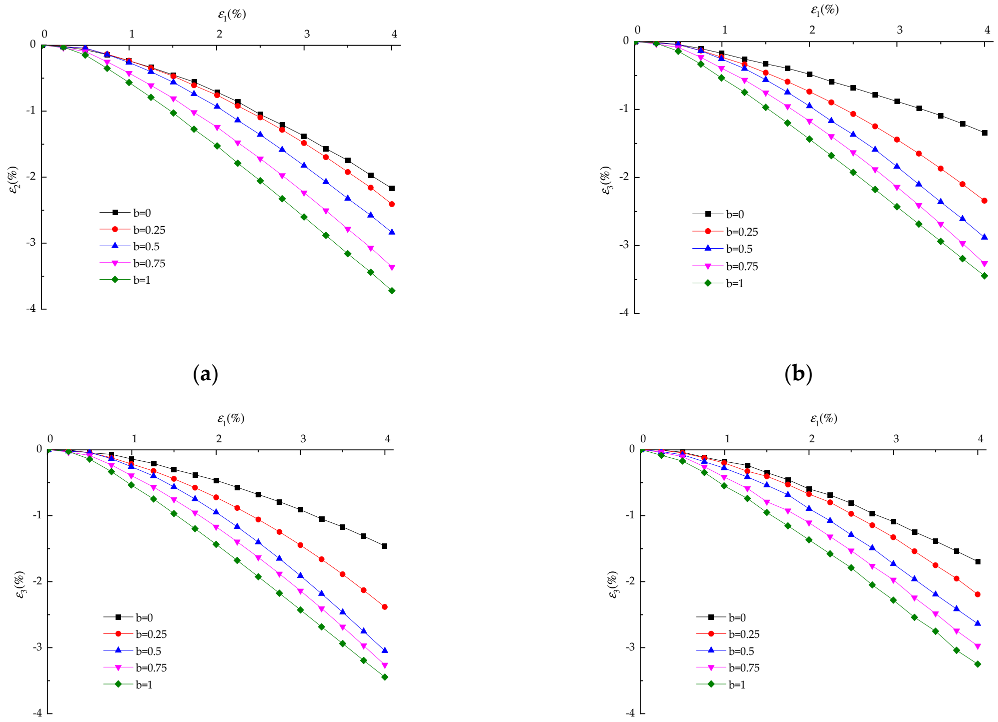

(**a**) (**b**)

(**c**) (**d**)

Figure 6. ε3~ε1 relationship curves under different confining pressure conditions: (**a**) σ3 = 20 Kpa; (**b**) σ3 = 40 Kpa; (**c**) σ3 = 60 KPa; (**d**) σ3 = 80 Kpa.

In Figure 6, it can be observed that under different confining pressures, the small principal strains exhibited by the soil were all negative, indicating a shear dilation behavior throughout the deformation process. Similarly, under identical confining pressure conditions, as the b-value increased, the minor strains also increased when aiming to achieve the same axial strain. Moreover, within the strain range of less than approximately 1.1%, the curve presents a relatively flat segment, suggesting restricted expansion in ε3. When the pressure amplifies and the axial strain exceeds this region, the curve's slope progressively augments. Such behavior is attributed to the initial compression of soil particles, resulting in heightened interlocking among particles. Upon reaching the soil's yield strength, particle sliding commences, causing substantial internal structural damage. Under unchanging b-value conditions, the absolute value of the curve's slope shows an inverse relationship with the transverse pressure. As the transverse pressure increases, the curve's slope decreases, and this reduction becomes less prominent. Furthermore, elevated confining pressures resulted in a denser distribution of the curves, signifying that a heightened confining pressure improved the stability of the soil structure and reduced sensitivity to variations in the b-value.

3.1.4. εv~ε1 Relationship Curve

Figure 7 depicts the εv~ε1 relationship curves of the compacted cured lightweight fill soil under different confining pressures.

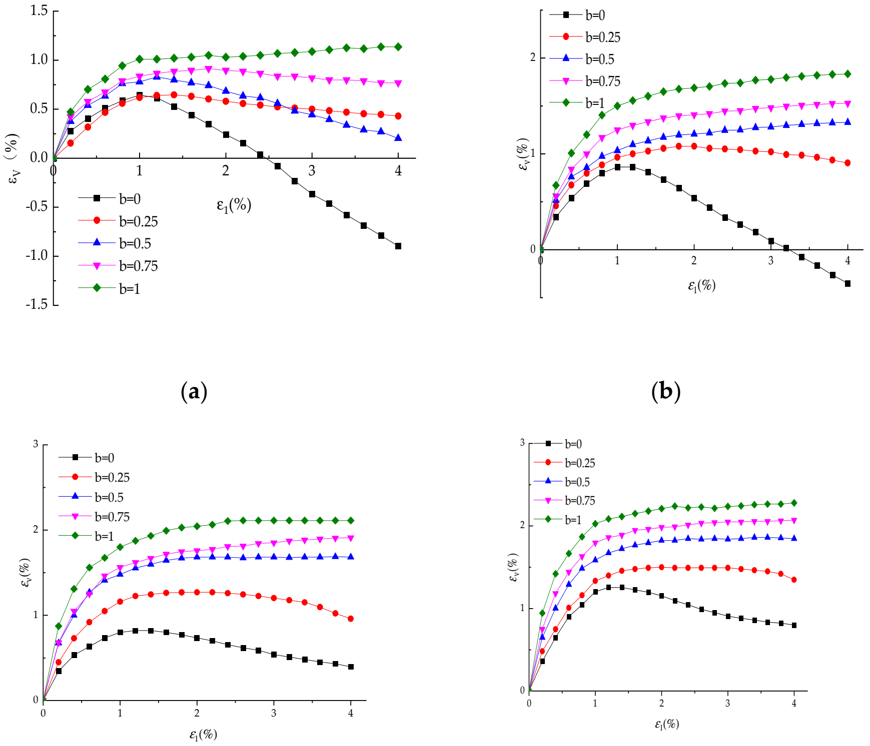

(**a**) (**b**)

(**c**) (**d**)

Figure 7. εv~ε1 relationship curves under different confining pressure conditions: (**a**) σ3 = 20 kPa; (**b**) σ3 = 40 kPa; (c) σ3 = 60 kPa; (**d**) σ_3 = 80 kPa.

The correlation between εv and ε1 under identical confining pressure conditions is depicted in Figure 7. Where εv represents the volumetric strain, the curve displays the following variation pattern: In the region where the axial strain is below 1.1%, rapid growth is observed. Within this range, the volume deformation showcases shear contraction behavior. Nevertheless, once the axial strain surpasses this range, the curve's slope markedly diminishes, eventually approaching a smooth straight line. This suggests that the soil manifested shear dilation characteristics. The trends in the curve changes corresponding to various confining pressures are fundamentally alike. However, with an increase in the transverse pressure, the shear expansion decreased. For transverse pressure below 40 kPa, the soil typically demonstrated shear dilation characteristics. Conversely, under elevated confining pressures, shear contraction behavior prevailed, portraying an overall shear contraction characteristic throughout the process. Under low confining pressure conditions (i.e., when the confining pressure was below 40 kPa), and b = 0, the soil underwent an initial contraction, followed by dilation as the axial strain increased. Upon reaching a specific level of axial strain, the soil's deformation shifted from compression to expansion in the direction of the volumetric strain, denoted by a negative εv. In this study, compression strain is defined as the positive direction, while tensile strain is considered the negative direction, illustrating soil expansion along this axis. Thus, when b = 0, a confining pressure of 40 kPa serves as the critical point for the deformation transition in the solidified lightweight soil. When the confining pressure fell below 40 kPa, as the contraction progressed, the deformation in the direction of the volumetric strain shifted from compression to expansion. Conversely, when the confining pressure surpassed 40 kPa, the soil's deformation in the direction of volumetric strain remained in compression with the increasing axial strain. This occurred because as the b value increased, the lateral constraint on the soil intensified, enhancing its strength. Specifically, when b = 0, the lateral constraint on the soil was minimal. At a low confining pressure during this phase, the soil could withstand the pressure imposed by the modest confining pressure. However, as the confining pressure rose, this resistance gradually diminished, leading to a transition in the soil's state from expansion to compression. Moreover, under identical confining pressure conditions, the shear dilation characteristics of the solidified lightweight soil tended to diminish with an increase in the b-value, while the shear contraction characteristics exhibited an upward trend. For low-confining-pressure conditions, with a continuous increase in the b-value, the soil initially demonstrated shear contraction, followed by transitioning to shear dilation. However, upon reaching a specific confining pressure value, the soil displayed shear contraction characteristics. As the confining pressure increased, the volume strain εv generated by the soil under the same axial strain ε1 also escalated. Furthermore, with an increase in the confining pressure, the curve's inflection point shifts to the right, denoting that heightened confining pressure augmented the soil's capacity to withstand external pressure, resulting in amplified axial strain and volumetric deformation.

3.1.5. Strength Parameters of Solidified Lightweight Soil

Utilizing the Mohr–Coulomb failure theory, the shear strength envelopes of the solidified lightweight soil were derived under various principal stress ratios. In this paper, the shear strength envelopes of the specimens are presented under diverse confining pressures and principal stress ratio (b) test conditions, with a density of ρ = 1.0ρ0. The shear strength envelope of the test specimen is illustrated in Figure 8 below. Here, c represents cohesion, and φ represents the internal friction angle.

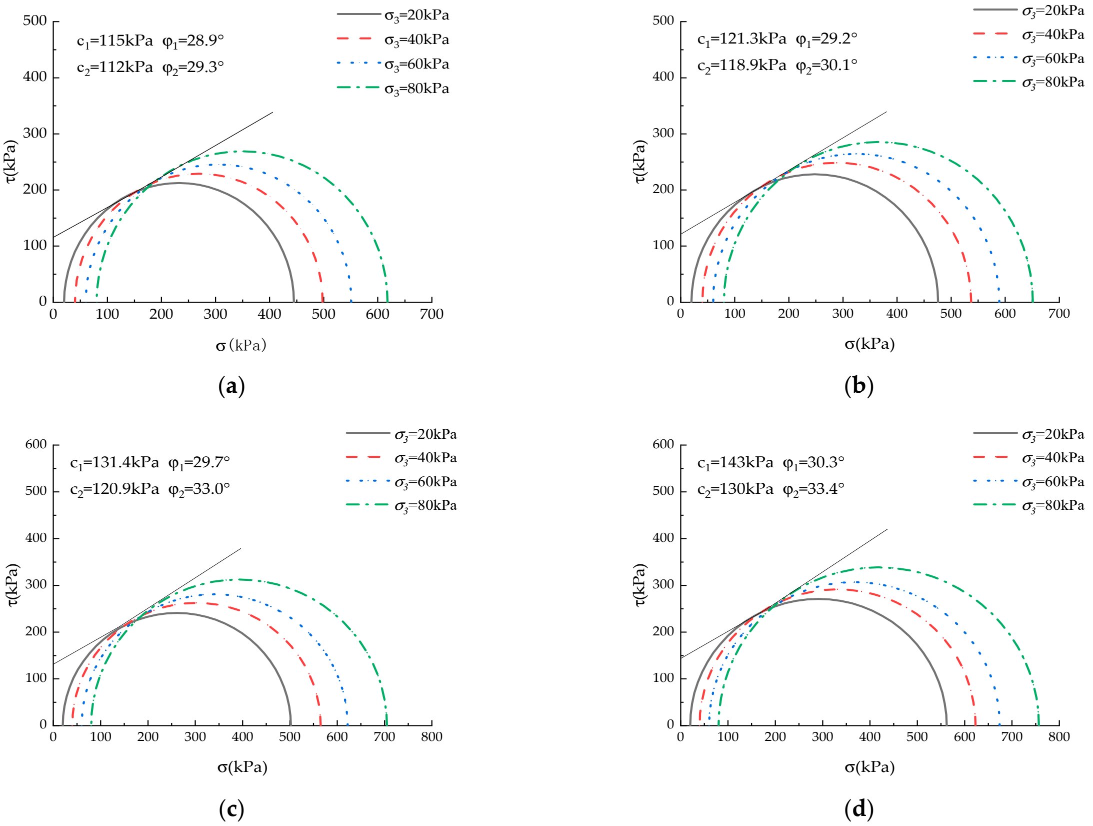

(a)

(b)

(c)

(d)

Figure 8. Shear strength curves under different conditions of principal stress ratios and equal σ3 and equal b tests: (**a**) b = 0.25; (**b**) b = 0.5; (**c**) b = 0.75; (**d**) b = 1.

Variations in the c value and φ value of the solidified lightweight soil under different b-values in the equal σ3 and equal b tests can be inferred from the shear strength envelope plot in Figure 8. Table 6 offers a concise overview of the c value and φ value of the solidified lightweight soil in conditions where σ3 and b were held equal.

Table 6. Soil strength parameters under equal σ3 and equal b tests.

Parameter		**b**				
		0	**0.25**	**0.5**	**0.75**	**1**
C (kPa)	First	103.7	115	121.3	131.4	143
	Second	100.5	112	118.9	120.9	130.2
φ (°)	First	26.1	28.9	29.2	29.7	30.3
	Second	27.5	29.3	30.1	33.0	33.4

In analyzing Table 4, it is clear that the Mohr circles' strength characteristics under the true triaxial test conditions at 20–80 kPa showcase a strength envelope characterized by a two-segment linear form. Notably, the strength parameters obtained from these two linear segments were relatively proximate. In order to comprehensively account for the influence of both segments, a least-squares fitting method was utilized to approximate them as a single straight line. This approximation yielded the fitted c values and φ values, as depicted in Figures 9 and 10.

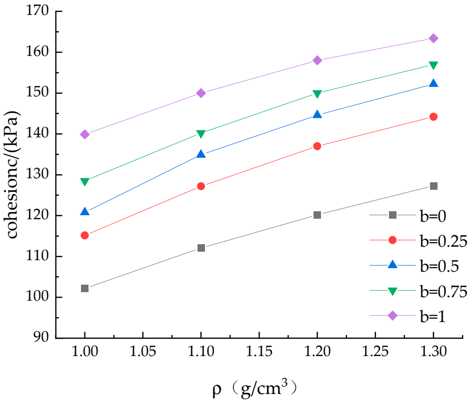

Figure 9. Curve of cohesion c with density.

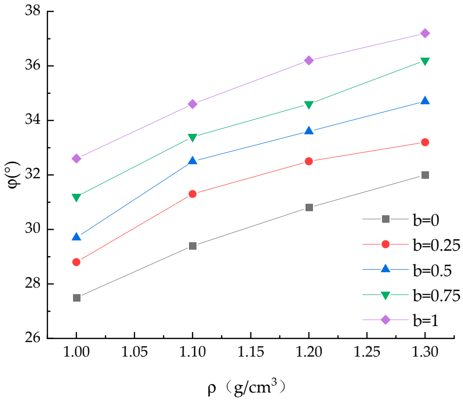

Figure 10. Curves of internal friction angle φ varying with density.

As evident from Table 6 and Figures 9 and 10, it is clear that under varying conditions of the principal stress ratio (b), an increase in density led to a noticeable rise in the c value and φ value for the compacted solidified lightweight soil. This phenomenon can be attributed to the greater number of soil particles within a denser soil mass, leading to stronger inter-particle connections. Additionally, higher-density solidified soil contains a higher concentration of curing agents and foaming agents, contributing to enhanced soil bonding to a certain extent. Consequently, the cohesion (c) of the solidified lightweight soil increased with increased density. Moreover, with an increase in the principal stress ratio (b), both the c value and φ value of the compacted solidified lightweight soil display an upward trend. The strength parameters acquired from true triaxial tests surpass those from the conventional triaxial tests, underscoring the notable impact of the transverse pressure ratio on the soil strength. This observation also implies that the c value and φ value derived from the conventional triaxial compression tests are on the conservative side. Given that shear failure primarily transpires on the σ1~σ3 plane, it is justifiable to overlook the impact of the principal stress.

Through an analysis of Figures 9 and 10, it is evident that the alteration in the strength characteristics, c value, and φ value under various principal stress ratio (b) values can be accurately described using Equations (1) and (2). These parameters are succinctly summarized in Tables 7 and 8, as depicted below. In this context, e signifies the base of the natural logarithm, serving as the foundation for the natural logarithm function. It aids in establishing the correlation between cohesion (c) and the internal friction angle (φ) strength indicators across varying b values amidst density fluctuations.

$$\mathrm{c} = \mathrm{A}e^{-\frac{\rho}{B}} + C \tag{1}$$

$$\varphi = \mathrm{A}e^{-\frac{\rho}{B}} + C \tag{2}$$

Table 7. Parameters of C-B curves of hydraulic solidified lightweight fill soil.

Cohesion	**Medium Principal Stress Ratio**	**Parameter**			**R^2**
/kPa	**b**	**A**	**B**	**C**	
c	0	165.00657	−342.49703	1.69658	0.99986
	0.25	170.4544	−669.16323	2.49269	0.99971
	0.5	171.42103	−854.62093	2.68030	0.99956
	0.75	173.52317	−736.69488	2.44751	0.99929
	1	179.80055	−788.90055	2.98318	0.99932

Table 8. Parameters of φ-B curves of reclaimed solidified lightweight soil.

Internal Friction Angle	**Medium Principal Stress Ratio**	**Parameter**			**R^2**
/°	**b**	**A**	**B**	**C**	
φ	0	36.22823	−96.32231	2.40211	0.99937
	0.25	36.60472	−131.31928	2.82521	0.99679
	0.5	37.81645	−308.17322	3.76722	0.99943
	0.75	38.82637	−216.10413	3.34794	0.99203
	1	39.09989	−383.19331	4.07753	0.99968

Equations (1) to (2) present mathematical expressions delineating the variation of the shear strength parameters, cohesion (c), and internal friction angle (φ), concerning the density (ρ) under diverse principal stress conditions. For a deeper understanding of the relationships among these parameters and the principal stress ratio (b), it is crucial to scrutinize the functional relationships between the b-values and the coefficients A, B, and C. As depicted in Tables 5 and 6, the alterations in parameters A, B, and C prove to be intricate with fluctuations in the principal stress ratio. Hence, a continued analysis was performed to fit these three parameters, yielding the subsequent fitting equations:

$$\mathrm{A} = \mathrm{m} + eb + fb^2 + gb^3 \tag{3}$$

$$\mathrm{B} = \mathrm{m} + eb + fb^2 + gb^3 \tag{4}$$

$$\mathrm{C} = \mathrm{m} + eb + fb^2 + gb^3 \tag{5}$$

Substituting the values from Tables 9 and 10 as well as Equations (3) to (5), into Equations (1) and (2), we obtained mathematical expressions for the shear strength characteristics, the c value and φ value, as functions of the two variable factors: principal stress ratio (b) and density (ρ). These expressions are presented as Equations (6) and (7):

$$\begin{aligned} \mathrm{c} = (8414.1083- \quad & 147.02716\mathrm{b} + 0.85551b^2 \\ & -0.00166b^3)e^{\frac{\rho}{30.91733+0.17288b+0.00003b^2-0.00002b^3}} - 12.149 \\ & +11.54429b - 3.64656b^2 + 0.39404b^3 \end{aligned} \tag{6}$$

$$\begin{aligned} \varphi = (-7721.285+ \quad & 615.1512\mathrm{b} - 16.3365b^2 \\ & +0.14463b^3)e^{\frac{\rho}{1.39231+0.02173b+0.00005b^2-0.00003b^3}} - 13.73148 \\ & +19.21545b - 8.89079b^2 + 1.37655b^3 \end{aligned} \tag{7}$$

Table 9. Parameters of the relationship curves between cohesive force c parameters A, B, and C and density.

Cohesion		**m**	**e**	**f**	**g**	**R^2**
c	A	8414.10839	−147.02716	0.85551	−0.00166	0.96314
	B	30.91733	0.17288	0.00003	0.000002	0.95775
	C	−13.73148	19.21545	−8.89079	1.37655	0.93915

Table 10. Parameters of internal friction angle φ of density curves of parameters A, B, and C.

Internal Friction Angle		**m**	**e**	**f**	**g**	**R^2**
φ	A	−7721.285	615.1512	−16.3365	0.14463	0.99423
	B	−1.39231	−0.02173	−0.00005	0.00003	0.95849
	C	−12.14954	11.54429	−3.64656	0.39404	0.98526

3.2. *Three-Dimensional Mechanical Behavior Study under Plane Strain Conditions*

3.2.1. Stress–Deformation Correlation

Figure 11 depicts the stress–deformation diagrams of the solidified lightweight soil under different confining pressure conditions when subjected to plane strain conditions.

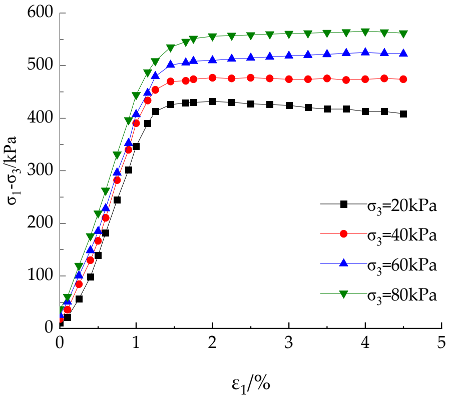

Figure 11. (σ1–σ3)~ε1 relationship curves under different confining pressure conditions.

By observing Figure 11, it is evident that the (σ1–σ3)~ε1 curves showcase comparable trends across various confining pressure conditions. Nonetheless, a distinct difference is evident in the curve related to a confining pressure of 20 kPa when compared to curves linked with higher confining pressures. This variation stems from the fact that, at lower confining pressures, the soil encountered reduced lateral constraint, struggling to effectively withstand external pressure. Consequently, once the soil reached its yield strength, there was a certain range of reduced deviatoric stress with increasing axial strain, resulting in a softening behavior in the strain. In contrast, as the transverse pressure increased, the average pressure exerted on the soil intensified, improving the sideways confinement of the soil structure. This resulted in further reinforcement of the soil structure. Therefore, when the soil reached its yield strength under higher confining pressures, the softening phenomenon weakened and may even have manifested as strain-hardening behavior. Figure 11 additionally illustrates that, before reaching an axial strain of 1.3%, as the transverse pressure rises, both the slope and maximum strength of the stress–deformation curve steadily rise, and the deviatoric stress needed to achieve identical axial strain also increases. For equivalent axial strains, the variation trend of the stress–strain relationship in the solidified lightweight soil mirrors that observed in the conventional triaxial and equal σ3 and equal b tests. Under lower confining pressures, there was no notable enhancement in the strength of the solidified lightweight soil within the 20 kPa to 40 kPa confining pressure range. However, upon reaching the 60 kPa to 80 kPa confining pressure range, there was a significant augmentation in strength, accompanied by an increase in the deviatoric stress.

3.2.2. Stress–Strain Relationship

Figure 12 depicts the Mohr circles representing the shear strength of the solidified lightweight soil under plane strain test conditions. Resembling the characteristics observed in the equal σ3 and equal b tests, the Mohr envelope in the plane strain test also showcases a piecewise linear form, although with a smaller included angle.

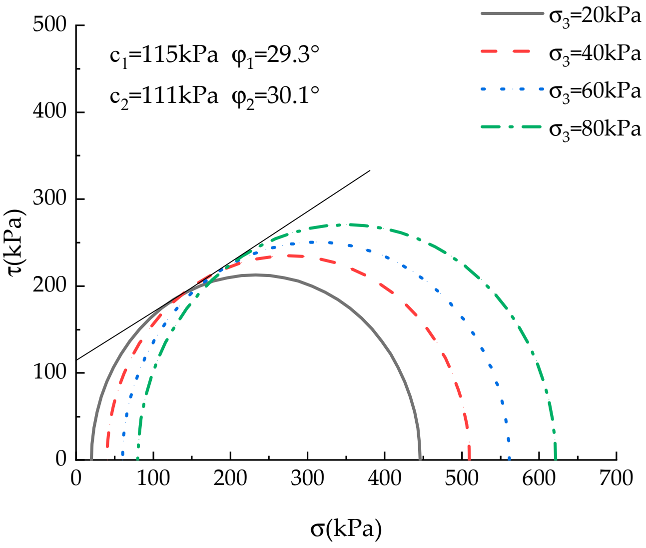

Figure 12. Mohr’s circle of plane strain testing.

As outlined in Table 11, the strength parameters derived from the plane strain tests surpass those obtained under the conventional triaxial test conditions (b = 0). Precisely, in the plane strain tests, the cohesion registered an approximate 10.7% increase, and the internal friction angle showed an approximate 11% increment compared to the conventional triaxial tests. This variation stems from the reality that, in plane strain tests, the middle major stress endured by the soil surpasses the major stress, yielding a higher average principal stress (p) in plane strain tests compared to conventional triaxial tests. The test outcomes also showcase that the strength parameters procured from the conventional triaxial tests are marginally conservative in comparison to true triaxial tests. Furthermore, the table elucidates that the discrepancy in cohesion between the two distinct paths of true triaxial tests is minimal. Nevertheless, the internal friction angle derived from the plane strain tests surpasses the values obtained in the equal σ3 and equal b tests. This is attributed to the substantial lateral confinement experienced by the soil in the plane strain tests, resulting in higher overall soil strength and greater compactness. Consequently, the inter-particle bonding within the soil is enhanced, leading to a higher internal friction angle.

Table 11. Comparison of soil strength parameters under plane strain test and equal σ3 and equal b tests.

Experiment type	**Parameter**		**b**				
			0	**0.25**	**0.5**	**0.75**	**1**
Equal σ3 and b test	C (kPa)	First	103.7	113.6	121.3	131.4	143
		Second	100.5	111.9	118.9	120.9	130.2
	φ (°)	First	26.1	28.9	29.2	29.7	30.3
		Second	27.5	29.3	30.1	33.0	33.4
Plane strain test	C (kPa)	First			115		
		Second			111		
	φ (°)	First			29.3		
		Second			30.1		

3.2.3. Comparative Analysis of Stress–Strain Relationships under Different Stress Paths

A comparative examination of stress–strain relationships, depicted by (σ1-σ3)~ε1 curves, was undertaken to scrutinize the strain behavior of the solidified lightweight soil under various stress trajectories and discern them from the conventional triaxial tests. Figures 13–15 depict comparative stress–strain curve plots of the conventional triaxial tests, alongside two distinctive stress paths in the true triaxial tests, under various confining pressures (σ3: 20–80 kPa).

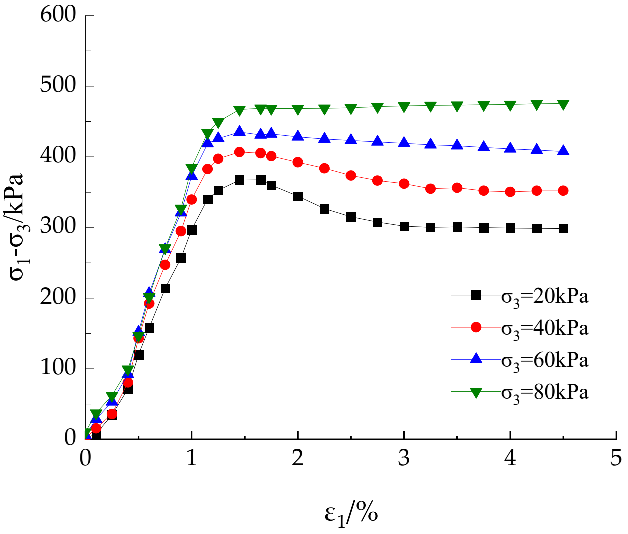

Figure 13. (σ1-σ3)~ε1 relationship curves of conventional triaxial stress of solidified lightweight soil under different confining pressures.

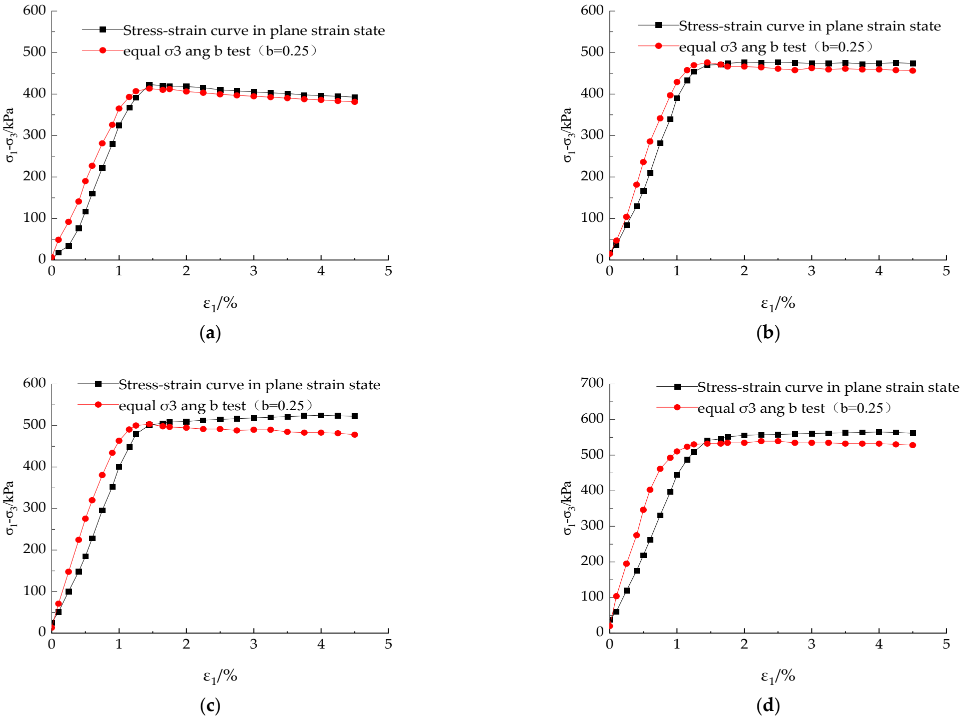

Figure 14. Comparison of (σ1-σ3)~ε curve relationships under different confining pressure conditions, equal σ3 and equal b tests and plane strain tests: (**a**) σ3 = 20 kPa; (**b**) σ3 = 40 kPa; (**c**) σ3 = 60 kPa; (**d**) σ3 = 80 kPa.

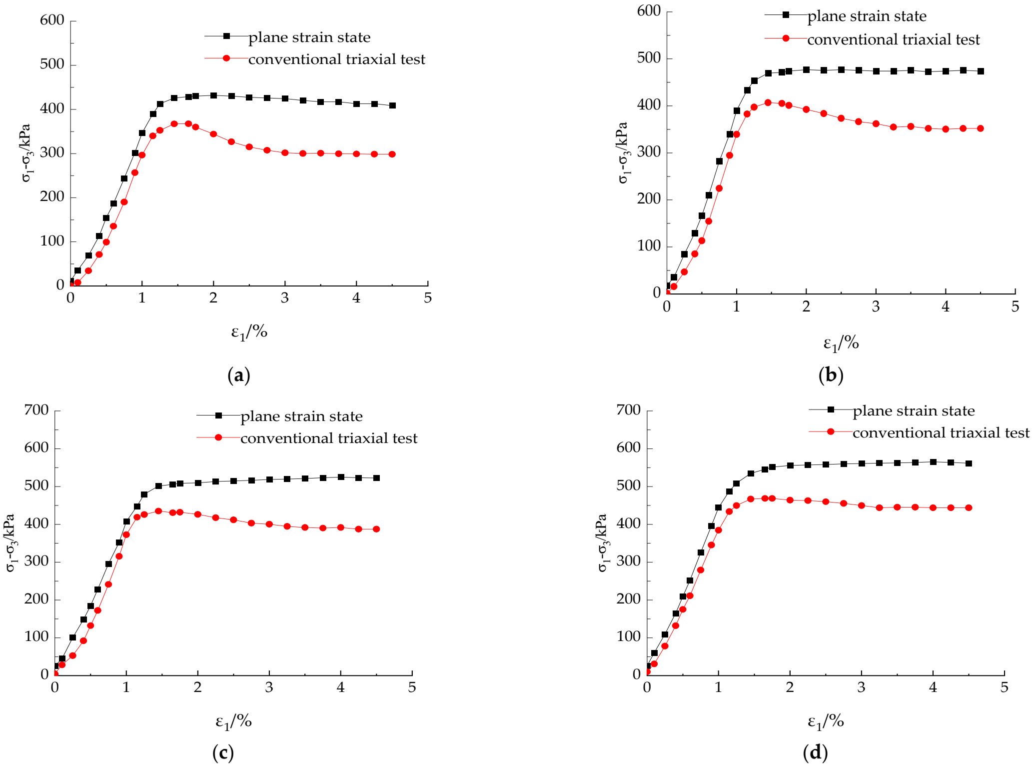

Figure 15. Comparison of (σ1-σ3)~ε1 curve relationships in conventional triaxial test and plane strain test under varying transverse pressure conditions: (**a**) σ3 = 20 kPa; (**b**) σ3 = 40 kPa; (**c**) σ3 = 60 kPa; (**d**) σ3 = 80 kPa.

As clearly shown in Figure 14, the stress–strain curve trends in both the equal σ3 and equal b tests and the plane strain tests exhibit fundamentally similar behaviors. Nevertheless, the curves from the equal σ3 and equal b tests display a slightly higher slope compared to the plane strain tests, signifying that achieving the same strain level demanded a higher deviatoric stress in the equal σ3 and equal b tests. Additionally, when comparing the stress–strain curves after the soil reached its yield strength, it becomes apparent that the strain-softening tendency in the plane strain path was somewhat weaker than that in the equal σ3 and equal b path. Figure 15 demonstrates that, before the soil reached its yield strength, the stress–deformation relationship plots from the tests conducted under the plane strain conditions and conventional triaxial experiments follow a similar trend. Nevertheless, the curve from the plane strain test exhibits a higher slope and a greater peak point in comparison to the curve from the conventional triaxial test. This indicates that, before yielding, the plane strain tests necessitated a higher deviatoric stress and greater stiffness to attain equivalent strains compared to the conventional triaxial tests. After reaching the yield strength, the behaviors of the two curves diverge. This suggests that, in practical engineering applications, soils under plane strain conditions demonstrate a higher load-bearing capacity than those tested under conventional triaxial conditions.

3.2.4. Relationship between Principal Strains

Figures 16 and 17 depict comparative εv~ε1 relationship curves under different confining pressures of plane strain tests, conventional triaxial tests, and equal σ3 and equal b tests with b = 0.25, respectively.

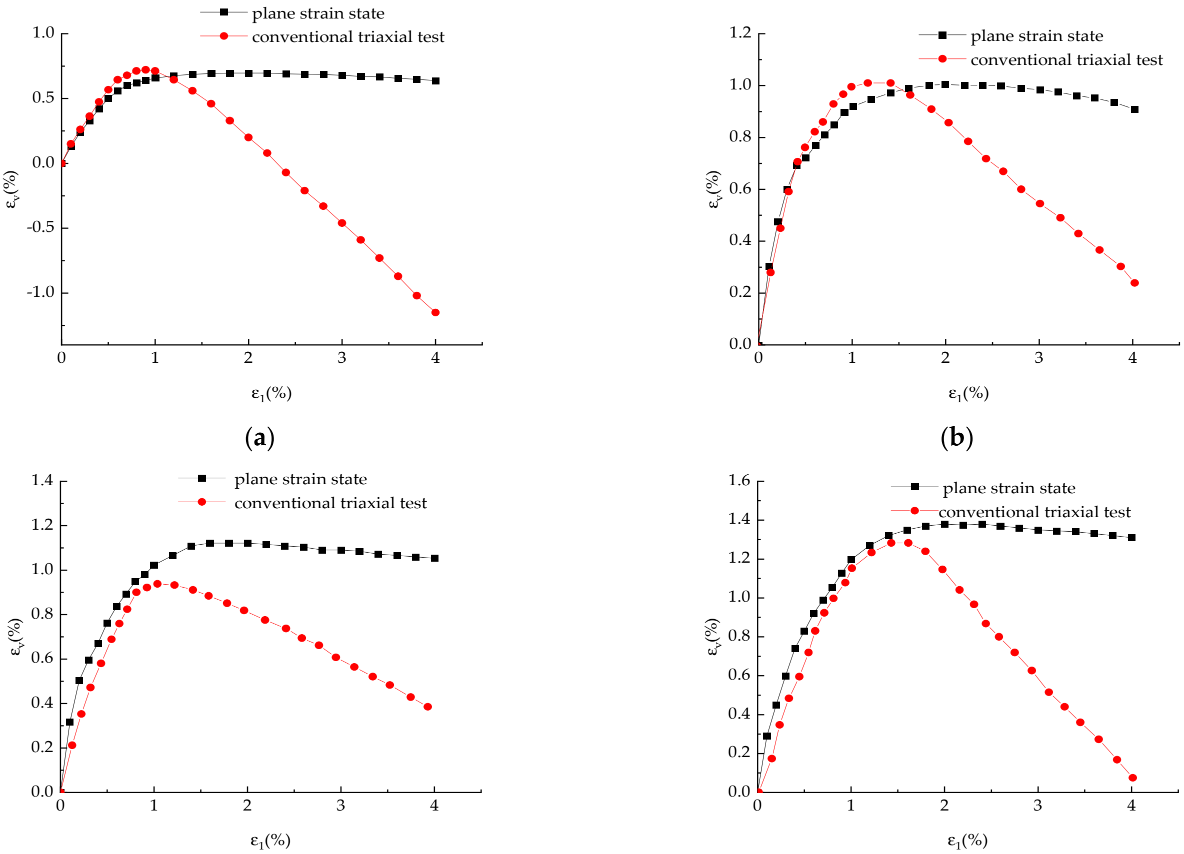

(**a**) (**b**)

(**c**) (**d**)

Figure 16. Comparison of $\varepsilon_v \sim \varepsilon 1$ relationship curves of conventional triaxial tests and plane strain tests under different confining pressures: (**a**) σ3 = 20 kPa; (**b**) σ3 = 40 kPa; (**c**) σ3 = 60 kPa; (**d**) σ3 = 80 kPa.

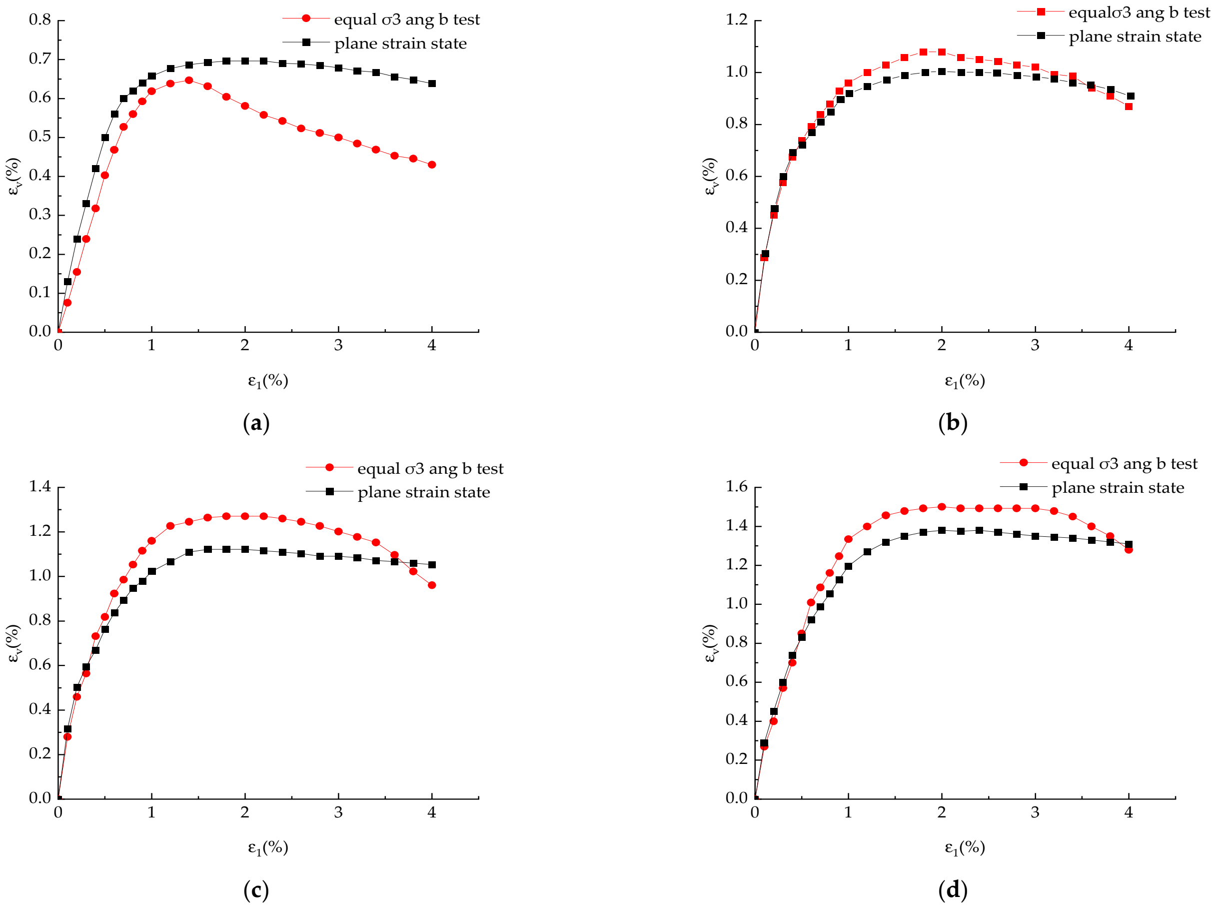

(**a**) (**b**) (**c**) (**d**)

Figure 17. Comparison of εv~ε1 relationship curves of true triaxial test and plane strain test under different confining pressures: (**a**) σ3 = 20 kPa; (**b**) σ3 = 40 kPa; (**c**) σ3 = 60 kPa; (**d**) σ3 = 80 kPa.

Figure 16 clearly shows that under varying confining pressure conditions, the deformation characteristics in the plane strain test and the conventional triaxial test markedly differ. This signifies that in the initial stages of strain, both tests had a linear increase in the volumetric strain εv with the axial strain ε1. Nevertheless, as the axial strain reached the yield point and attained the same axial strain ε1, the plane strain test yielded a greater volumetric strain εv compared to the conventional triaxial test. This disparity arose from the plane strain test restricting the lateral deformation of the soil, initially causing shear dilation deformation solely in the direction of the minor principal stress. In contrast, the conventional triaxial test permitted shear dilation deformation in both stress directions, resulting in a more pronounced shear dilation behavior compared to the plane strain test. In observing Figure 17, it is clear that, excluding the curve at a transverse pressure of 20 kPa, the εv~ε1 curves from the equal σ3 and equal b tests consistently lie above the curves from the plane strain test. Moreover, both types of tests display a shared characteristic where the volumetric strain εv initially rises and then declines with an increase in the major stress. This suggests that the soil experienced a phase of shear contraction, followed by shear dilation. However, the extent of change in the volumetric strain during the shear dilation phase was significantly less in the plane strain test compared to the equal σ3 and equal b test.

Figures 18 and 19 present comparisons of the ε3~ε1 relationship curves between the plane strain test under different confining pressures and the equal σ3 and equal b test with b = 0.25, respectively.

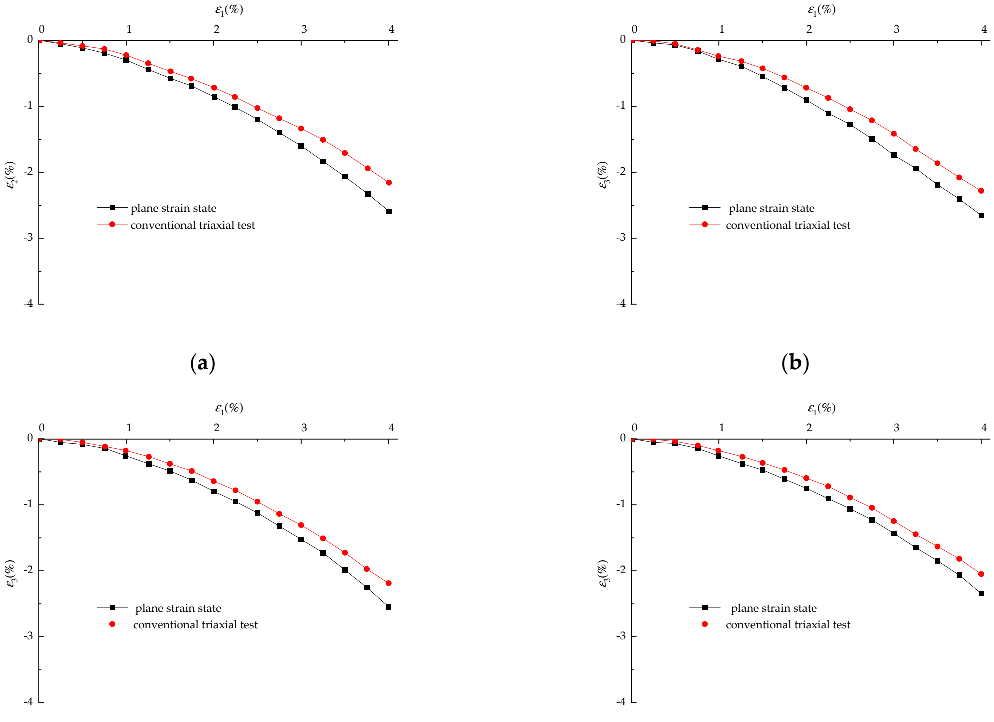

(**a**) (**b**) (**c**) (**d**)

Figure 18. Comparison of ε3~ε1 relationship curves of plane strain test and conventional triaxial test: (**a**) σ3 = 20 kPa; (**b**) σ3 = 40 kPa; (**c**) σ3 = 60 kPa; (**d**) σ3 = 80 kPa.

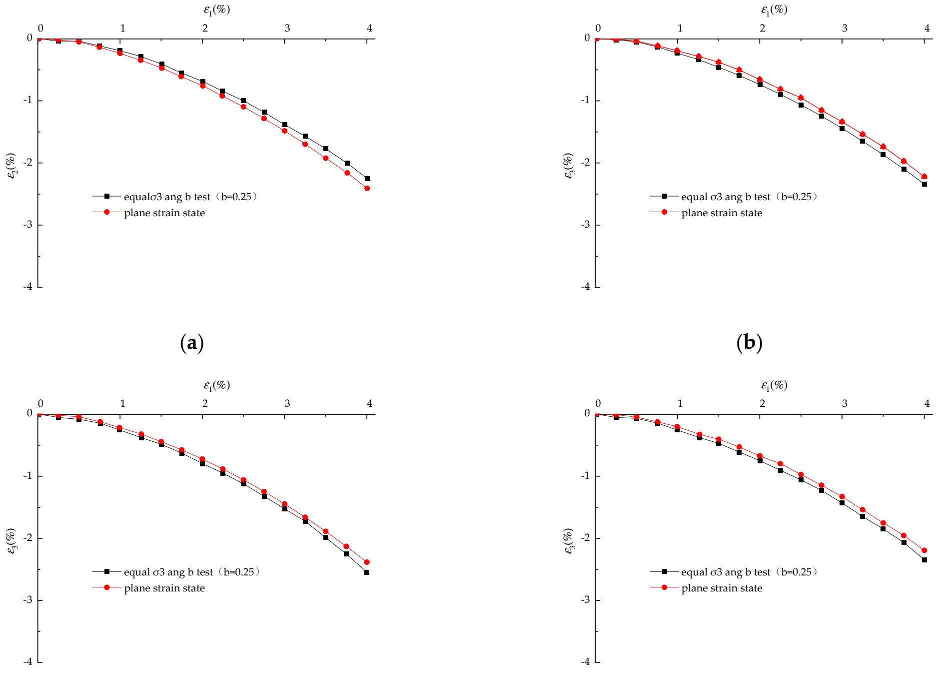

(**a**) (**b**) (**c**) (**d**)

Figure 19. Comparison of ε3~ε1 relationship curves of plane strain test and equal σ3 and equal b test: (**a**) σ3 = 20 kPa; (**b**) σ3 = 40 kPa; (**c**) σ3 = 60 kPa; (**d**) σ3 = 80 kPa.

In examining Figures 18 and 19, it is apparent that the ε3~ε1 curves from the plane strain test, under varying confining pressures, follow a comparable pattern of change with those from the conventional triaxial test and the equal σ3 and equal b test. In particular, with increasing major principal strain, all curves display a tendency for shear dilation along the direction of the smaller principal strain. For relatively low major principal strains, the curves are quite flat, characterized by small absolute slope values. However, with an increase in the major principal strain, the absolute slope values of the curves gradually rise. The ε3~ε1 curves from the plane strain test bear a strong resemblance to those of the equal σ3 and equal b test, with the exception of the curve at a transverse pressure of 20 kPa. Consequently, when the soil experienced the same major principal strain, the plane strain test yielded a smaller minor principal strain compared to the equal σ3 and equal b test.

3.3. Constitutive Model for Cured Lightweight Soil under Three-Dimensional Mechanical Conditions

3.3.1. Parameter Determination

From the compression tests, the compression index Cc and the rebound index Cs for different densities were obtained. Specifically, λ = 0.434 Cc and κ = 0.434 Cs. The value of ν, which represents the absolute ratio of lateral strain to axial strain, as determined from the ε3~ε1 relationship curves obtained through the genuine triaxial tests. In the earlier sections, the strength parameters for the cured lightweight soil under various stress trajectories in the genuine triaxial tests were presented. Therefore, the parameter M can be determined as follows, where the critical state stress ratio is denoted as:

$$\mathrm{M} = \frac{6\sin\varphi}{3-\sin\varphi} \tag{8}$$

By incorporating the middle principal stress ratio (b) and density (ρ) into the model, we established the relationship between the internal friction angle (φ) and these factors to reflect their influence on the prediction curve. The critical state stress ratio (M) is also related to the middle principal stress ratio (b) and density (ρ). By incorporating the modified Cambridge model parameters related to the three-dimensional mechanical properties into the modified Cambridge curve model, we obtained the corresponding prediction curves. We considered conditions where the density ρ = 1.0ρ0 and middle principal stress ratio was from b = 0.25 to b = 1, and conditions where b = 0.5 with densities ρ = 1.1ρ0 and ρ = 1.3ρ0. The model parameters are presented in Tables 12–14.

Table 12. Parameters of Cambridge model for solidified lightweight soil: Case 1.

ρ	b	λ/(1 + e0)	k/(1 + e0)	φ	M	ν
ρ = 1.0ρ0	0.25	0.034	0.0035	28.9	1.14	0.3
	0.5	0.034	0.0035	29.2	1.17	0.3
	0.75	0.034	0.0035	29.7	1.19	0.3
	1	0.034	0.0035	30.3	1.20	0.3
ρ = 1.1ρ0	0.5	0.033	0.0035	31.0	1.26	0.3
ρ = 1.3ρ0	0.5	0.030	0.0035	33.4	1.35	0.3

Table 13. Parameters of Cambridge model for solidified lightweight soil: Case 2.

ρ	b	λ/(1 + e0)	k/(1 + e0)	φ	M	ν
ρ = 1.0ρ0	0.25	0.034	0.0035	29.3	1.17	0.3
	0.5	0.034	0.0035	30.1	1.21	0.3
	0.75	0.034	0.0035	33.0	1.33	0.3
	1	0.034	0.0035	33.4	1.35	0.3
ρ = 1.1ρ0	0.5	0.033	0.0035	33.2	1.34	0.3
ρ = 1.3ρ0	0.5	0.030	0.0035	35.6	1.44	0.3

Table 14. Parameters of Cambridge model for solidified lightweight soil: Case 3.

ρ	b	λ/(1 + e0)	k/(1 + e0)	φ	M	ν
ρ = 1.0ρ0	0.25	0.034	0.0035	28.4	1.12	0.3
	0.5	0.034	0.0035	29.3	1.17	0.3
	0.75	0.034	0.0035	31.7	1.27	0.3
	1	0.034	0.0035	32.1	1.29	0.3
ρ = 1.1ρ0	0.5	0.033	0.0035	32.1	1.29	0.3
ρ = 1.3ρ0	0.5	0.030	0.0035	34.5	1.39	0.3

3.3.2. Verification of the Model by Test Results

By comparing the model validation with three sets of strength parameters, it was observed that the differences were relatively minor. Therefore, for model validation purposes, the strength parameters obtained through the least squares fitting were selected, as shown in Figures 20 and 21.

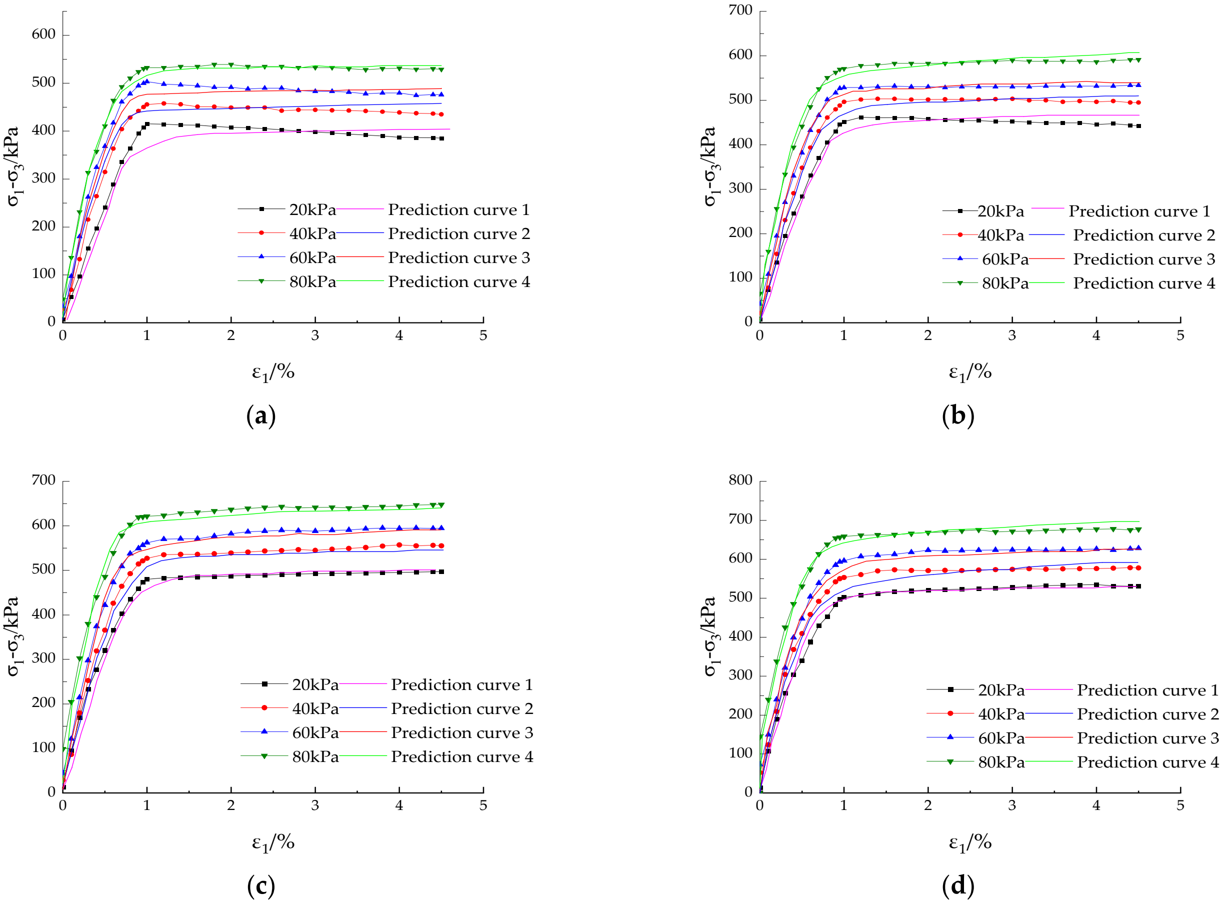

(**a**) (**b**) (**c**) (**d**)

Figure 20. Stress–deformation curves and modified Cambridge model prediction curves under different b-values: (**a**) b = 0.25; (**b**) b = 0.5; (**c**) b = 0.75; (**d**) b = 1.

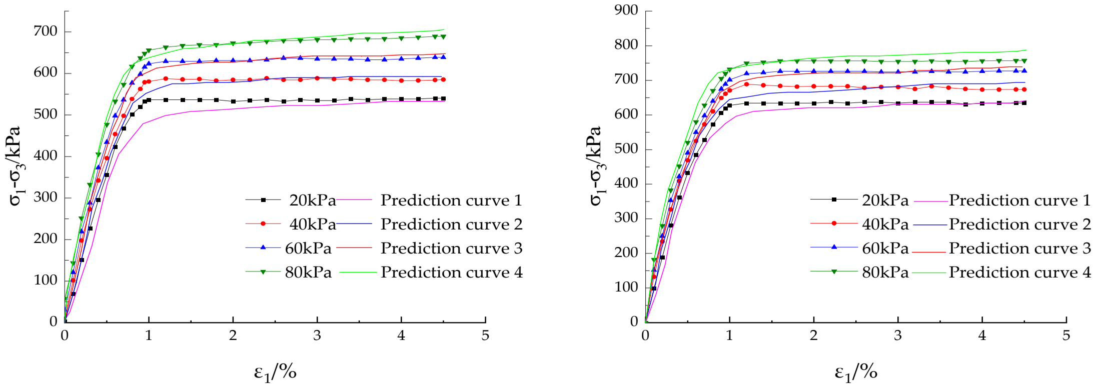

(**a**) (**b**)

Figure 21. Stress–strain curves and modified Cambridge model prediction curves under different density conditions: (**a**) ρ = 1.1 ρ0; (**b**) ρ = 1.3 ρ0.

To further validate the experimental results under the plane strain test circumstances, the model coefficients are presented in Table 15, and the validation curves are illustrated in Figure 22.

Table 15. Parameters of Cambridge model for solidified lightweight soil under plane strain test conditions.

ρ	λ/(1 + e0)	k/(1 + e0)	φ	M	ν
ρ = 1.0 ρ0	0.034	0.0035	29.3 30.1 29.8	1.17 1.21 1.19	0.3

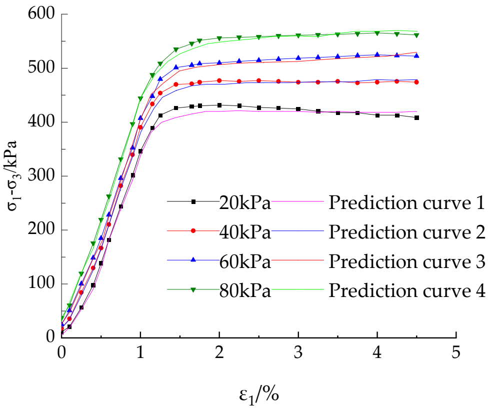

Figure 22. Stress–strain curves and modified Cambridge model prediction curves under plane strain conditions.

Figures 20–22 show a notable deviation between the experimental data and the predicted curve at a confining pressure of 20 kPa. However, under high-confining-pressure conditions, the Cambridge prediction model curve aligns closely with the true triaxial test curve. Moreover, with increasing confining pressure, the deviation between the two curves gradually reduces. This phenomenon can be attributed to the fact that higher confining pressure resulted in greater lateral constraints on the soil, strengthening the soil structure and overall increasing its strength. From the graphs, it is evident that the alignment between the prediction curve of the high-density soil in the model and the true triaxial test curve is superior compared to that of the low-density soil. This can be attributed to the fact that increased soil density corresponds to higher strength. Additionally, it is noteworthy that the alignment between the model's predicted curve and the plane strain path is superior compared to the equal σ3 and equal b test curve. In the plane strain test, the lateral strain was restricted, weakening the soil's tendency to undergo strain-softening.

3.4. Discussion

Several researchers have conducted a multitude of experiments on diverse soil types. However, research on highly saturated soft soils resulting from a combination of wastewater and waste soil is relatively scarce. Moreover, in the context of treating soft soils comprising waste soil and wastewater, the predominant scholarly focus centers on solidifying agent treatments, although the mechanisms of solidification differ. This article primarily emphasizes the utilization of silicate cement to treat a mixture of waste soil and wastewater, resulting in enhanced strength in the binding materials. Additionally, quicklime is employed for treating the waste soil and wastewater, creating an alkaline environment that facilitates a reaction between the foaming agent and water. The precise reaction mechanisms are delineated below: Upon mixing the waste soil with a slurry of silicate cement and wastewater, specific clinker minerals, including tricalcium silicate, β-C2 S, tricalcium aluminate, and solid iron phase solution, undergo a chemical reaction with the wastewater within the mixture. This reaction produces gel-like substances. These substances subsequently engage with the waste soil, resulting in a cementing effect, and thereby imparting a degree of strength to the waste soil + wastewater + cementitious material system. When quicklime is mixed with the blow-fill waste soil + wastewater, a chemical reaction ensues between the quicklime and water, resulting in the formation of lime water. This reaction is exothermic and proceeds rapidly. During this reaction, calcium oxide present in the quicklime reacts with hydroxide ions in the water, yielding calcium hydroxide and releasing a substantial amount of heat. In addition to the heat generated, this reaction establishes a conducive alkaline environment for the foaming agent. The alkaline conditions, coupled with the released heat, accelerate the reaction rate between the foaming agent and water. Hence, when mixing water with cement, quicklime, and blow-fill soft soil, a specific reaction takes place, enhancing the reaction rate of the foaming agent. These two solidifying agents contribute significantly to enhancing strength during the production of lightweight soil. Many researchers typically employ solid waste materials like slag, steel slag, and gypsum, along with alkaline activators, for treating soft soil resulting from the combination of waste soil and wastewater. Shen et al. [1] demonstrated a mechanism for treating soft soil involving the promotion of slag hydration by gypsum powder. Simultaneously, SO_4^{2-} reacts with hydrated calcium aluminate to produce AFt. AFt efficiently occupies soil pores, establishing a vital spatial network structure that reinforces soil stability. Yang et al. [2,3] decreased the solidifying agent dosage by incorporating varying amounts of fly ash as a solidifying agent in dredger filling. This reduction is attributed to the adherence of hydration products, particularly calcium aluminate resulting from the hydration reaction, to the particle surfaces and the subsequent filling of interparticle gaps. Lei et al. [4] used a chemical additive, polyacrylamide (APAM), to enhance the strength of solidified soil in high-water-content soil treatment. The application of APAM can accelerate the dissipation of excess pore pressure, achieving the purpose of enhanced strength.

In summary, in the treatment of mixtures of waste soil and wastewater, researchers often employ alkali activation to induce substances like slag, fly ash, and gypsum to generate Aft for strength enhancement. Alternatively, chemical additives like polyacrylamide are used to treat the waste soil and wastewater mixture. This focus is primarily on in situ treatment and does not encompass lightweight solidification technology. However, in this study, we primarily utilized a combination of cement and lime with a foaming agent. This choice was made considering the potential application of lightweight technology to the waste soil and wastewater mixture. This allows the wastewater, waste soil, solidifying agent, and foaming agent to form a new solidified lightweight material with enhanced strength. The resulting new solidified lightweight material is versatile and can be used in various applications, including as roadbed fillers. Differences in the solidification materials and mechanisms lead to distinctions in the three-dimensional mechanical properties and constitutive model studies of solidified soil. In this study, we conducted true triaxial experiments to investigate the three-dimensional mechanical properties of lightweight solidified soil and a constitutive model of solidified soil. This research fills the gap in the research on the constitutive model of solidified lightweight soil, particularly as a new type of roadbed filler.

Further research is necessary to explore the stress–strain curves of lightweight solidified soil under high-confining-pressure conditions, considering the increasingly complex and variable situations encountered in actual engineering. Additionally, investigating the effect of shear dilation on soil under high-confining-pressure conditions is crucial. Comparing and modifying the Cambridge model based on these conditions warrants attention. The study of soil constitutive models requires in-depth research, especially to consider the structural characteristics of the soil. The theoretical foundation of the Cambridge model is well-established, allowing for analysis in terms of finite elements. Exploring an open finite element platform for further development of the existing theoretical models is essential for achieving a simpler and clearer constitutive model of soil, which will guide engineering practices more effectively.

4. Conclusions

This study employed the fill soil resulting from the accumulation of waste soil and wastewater in Binhai New Area, Tianjin, as its primary material. To enhance its strength characteristics, appropriate additives were introduced. The optimal mixing ratio was determined through an orthogonal experimental method, followed by an in-depth examination of the stress–deformation interaction of the solidified lightweight fill soil. Various and comprehensive indoor basic mechanical tests, true triaxial tests, and plane strain tests were conducted on the solidified lightweight fill soil. Consequently, the constitutive relationships of the solidified lightweight fill soil were explored, yielding the following primary conclusions:

(1) During triaxial tests with equal stress (σ3) and equal b values, maintaining a constant confining pressure, the soil's strength was augmented with rising b values, leading to a diminishing softening trend in the curve. When the b values and density were held steady, the shear stress gradually escalated as the transverse pressure increased, manifesting a steeper curve slope and indicating an elevation in the initial shear modulus. Under identical transverse pressure and principal stress ratio (b) circumstances, the yield strain of the compacted lightweight soil was amplified with heightened density. Moreover, an escalation in the density corresponded to an increase in both the yield point and the peak of the compacted lightweight soil. For all b values and confining pressure conditions, the minor principal strain ε3 consistently maintained a state of shear dilation throughout the entire duration of the test. The volumetric strain εv demonstrated an initial pattern of shear contraction, followed by shear dilation. Furthermore, as the confining pressure gradually rose, the shear contraction behavior weakened.

(2) During triaxial tests with equal stress (σ3) and equal b values, the strength parameters of the soil surpassed those observed under the conventional triaxial conditions and escalated with increasing b values. The Mohr–Coulomb strength envelope of the compacted lightweight soil can be depicted as comprising two ascending straight-line segments. The parameters c and φ of the compacted lightweight soil increased with rising b values and an exponential growth with increasing density.

(3) In the plane strain test, the soil's strength slightly exceeded that of the equal σ3 and equal b test at b = 0.25 and the conventional triaxial test. The cohesion in the plane strain test exceeded that of the conventional triaxial test by 10.7%, while the internal friction angle showed an increase of 11%. When comparing the plane strain test to the equal σ3 and equal b test (b = 0.25), the cohesion values obtained were similar, but the

internal friction angle in the plane strain test was greater than that in the equal σ3 and equal b test.

(4) Compared to conventional triaxial tests, the peak strength in the plane strain test was higher, and residual deformation was less pronounced, indicating the soil's ability to withstand greater pressure under plane strain loading conditions. Under varying confining pressures, ε3 in the plane strain test showed a shear-dilation trend. Initially, εv experienced shear contraction followed by shear dilation, leading to larger εv values and weaker shear dilation behavior compared to the conventional triaxial tests.

(5) The enhanced modified Cambridge model, featuring its adjusted curve, closely mirrors the curves derived from true triaxial tests. It adeptly characterizes the stress–deformation response of the soil subjected to three-dimensional stress circumstances, offering a robust theoretical foundation for the practical implementation of lightweight stabilized soil in engineering projects.

Author Contributions: Conceptualization, A.Y.; methodology, A.Y.; software, J.X.; validation, C.X.; formal analysis, A.Y.; investigation, C.X.; resources, A.Y.; data curation, J.X.; writing—original draft preparation, J.X.; writing—review and editing, J.X.; visualization, A.Y.; supervision, A.Y.; project administration, J.X.; funding acquisition, A.Y. All authors have read and agreed to the published version of the manuscript.

Funding: This project was supported by the National Natural Science Foundation of China (No. 42177119, 51978440) and the Fundamental Research Funds for the Central Universities (No.2232021A-07).

Data Availability Statement: All of the data are contained within the article, whose results were obtained from the laboratory analysis.

Acknowledgments: We express our gratitude for the support provided by the School of Environmental Science and Engineering at Donghua University. Additionally, we extend our appreciation to Tianjin Chengjian University and the Key Laboratory of Soft Soil Characteristics and Engineering Environment in Tianjin for their valuable support.

Conflicts of Interest: The authors declare that there are no conflict of interest regarding the publication of this paper.

References

1. Yupeng, S.; Ping, L.; Peng, J.; Ying, L.; Ruiling, F.; Xin, L. Experiment and Mechanism Analysis on the Solidification of Saline Dredger Fill with Composite Slag Solidifying Agent: A Case Study in Caofeidian, China. *Appl. Sci.* **2022**, *12*, 1849.
2. Shuai, Y.; Wenbai, L.; Hongwei, L. Quantitative Analysis of the Relationship between Shear Strength and Fractal Dimension of Solidified Dredger Fill with Different Fly Ash Content under Monotonic Shear. *Pol. Marit. Res.* **2018**, *25*, 132–138. [CrossRef]
3. Yang, S.; Liu, W.B. The Effect of Changing Fly Ash Content on the Modulus of Compression of Stabilized Soil. *Materials* **2019**, *12*, 2925. [CrossRef]
4. Lei, H.; Xu, Y.; Li, X.; Jiang, M.; Liu, L. Effect of Polyacrylamide on Improvement of Dredger Fill with Vacuum Preloading Method. *J. Mater. Civ. Eng.* **2019**, *31*, 04019193. [CrossRef]
5. Li, J.; Tian, L.J.; Xu, Y.; Tian, Z.F.; Zhang, Z.D. Study on the Solidification Effect of Dredger Fill by Microbial-Induced Calcium Precipitation (MICP). *Materials* **2022**, *15*, 7891. [CrossRef]
6. Soganci, A.S.; Yenginar, Y.; Orman, A. Geotechnical Properties of Clayey Soils Stabilized with Marble Dust and Granulated Blast Furnace Slag. *KSCE J. Civ. Eng.* **2023**. [CrossRef]
7. Jia, Y.; Hua, S.; Qian, L.; Ren, X.; Zuo, J.; Zhang, Y. Development of Steel Slag-Based Solidification/Stabilization Materials for High Moisture Content Soil. *J. Renew. Mater.* **2022**, *10*, 735. [CrossRef]
8. Cui, C.; Yu, C.; Zhao, J.; Zheng, J.; Liu, F. Effect of steel slag on foam drying and carbonation properties of dredged slurry-dried soil mixtures. *Acta Geotech.* **2023**. [CrossRef]
9. Shi, J.; Wang, S.; Cao, W.; Su, J.; Zhang, X. Mechanical Properties and Strengthening Mechanism of Dredged Silty Clay Stabilized by Cement and Steel Slag. *Materials* **2022**, *15*, 3823. [CrossRef] [PubMed]
10. Huang, K.; Ma, Q.Y.; Cai, G.J.; Ma, D.D.; Yao, Z.M.; Zhang, H.P. Influence of intermediate principal stress ratio on strength and deformation characteristics of frozen sandy soil under different moisture contents. *Cold Reg. Sci. Technol.* **2023**, *213*, 103909. [CrossRef]
11. Rong, C.X.; Wang, Z.; Cao, Y.; Yang, Q.; Long, W. Orthogonal Test on the True Triaxial Mechanical Properties of Frozen Calcareous Clay and Analysis of Influencing Factors. *Appl. Sci.* **2022**, *12*, 8712. [CrossRef]

12. Zheng, F.; Shao, S.J.; Wang, Y.X.; Shao, S. A New Suction-Controlled True Triaxial Apparatus for Unsaturated Soil Testing. *Geotech. Test. J.* **2021**, *44*, 833–850. [CrossRef]
13. Gu, C.; Gu, Z.Q.; Cai, Y.Q.; Wang, J.; Dong, Q.Y. Effects of Cyclic Intermediate Principal Stress on the Deformation of Saturated Clay. *J. Geotech. Geoenviron. Eng.* **2018**, *144*, 04018052. [CrossRef]
14. Zheng, F.; Shao, S.J.; Wang, J.; Shao, S. Experimental Study on the Mechanical Behaviour of Natural Loess Based on Suction-Controlled True Triaxial Tests. *KSCE J. Civ. Eng.* **2020**, *24*, 2304–2321. [CrossRef]
15. Han, Y.; Kato, S.; Kim, B.S. DEM Analysis of Fabric Evolution and Behavior of Granular Geomaterials in True Triaxial Test with Flexible Boundary. *KSCE J. Civ. Eng.* **2023**, *27*, 3341–3354. [CrossRef]
16. Li, X.F.; Lu, W.N.; Ma, Z.G.; Tuo, N. The Undrained Characteristics of Tengger Desert Sand from True Triaxial Testing. *Adv. Civ. Eng.* **2021**, *2021*, 6320397. [CrossRef]
17. Shao, S.J.; Chen, F.; Shao, S. Shear Band Formation and Strength of Loess in True Triaxial Tests. *J. Test. Eval.* **2019**, *47*, 3003–3016. [CrossRef]
18. Zhang, K.Y.; Charkley, F.N. An anisotropic constitutive model of geomaterials based on true triaxial testing and its application. *J. Cent. S. Univ.* **2017**, *24*, 1430–1442. [CrossRef]
19. Cabrejos-Hurtado, J.; Galindo Torres, S.; Pedroso, D.M. Assessment of the Mechanical Behaviour of Granular Media by DEM-Based True Triaxial Tests. *Appl. Mech. Mater.* **2016**, *846*, 428–433. [CrossRef]
20. Salimi, M.J.; Lashkari, A. Undrained true triaxial response of initially anisotropic particulate assemblies using CFM-DEM. *Comput. Geotech.* **2020**, *124*, 103509. [CrossRef]
21. Ren, B.A.; Wang, T.J.; Xu, J.Y.; Wang, Z.H.; Lv, Y.; Ning, Y.P. Research on the True Triaxial Mechanical Properties of Concrete under the Coupling Action of High Temperature and Biaxial Unequal Lateral Pressure. *Materials* **2022**, *15*, 5014. [CrossRef]
22. Cao, Y.; Rong, C.X.; Wang, Z.; Shi, X.; Wang, B.; Long, W. Experimental Study on True Triaxial Mechanical Properties of Frozen Calcareous Clay under the Influence of Multiple Factors. *Crystals* **2022**, *12*, 328. [CrossRef]
23. Shao, S.; Shao, S.J.; Wang, J. True triaxial mechanical properties of unsaturated loess in foundation pit engineering. *Bull. Eng. Geol. Environ.* **2021**, *80*, 4751–4772. [CrossRef]
24. Shao, S.J.; Wang, Y.X.; Shao, S. A Large-Scale True Triaxial Apparatus with Rigid-Flexible-Flexible Boundary for Granular Materials. *Geotech. Test. J.* **2021**, *44*, 1179–1196. [CrossRef]
25. Andreghetto, D.H.; Festugato, L.; Miguel, G.D.; da Silva, A. Automated true triaxial apparatus development for soil mechanics investigation. *Soils Rocks* **2022**, *45*, e2022077321. [CrossRef]
26. Sun, Y.; Sumelka, W. State-dependent fractional plasticity model for the true triaxial behaviour of granular soil. *Arch. Mech.* **2019**, *71*, 23–47. [CrossRef]
27. Foroutan, T.; Mirghasemi, A.A. Use of CFD-DEM to evaluate the effect of intermediate stress ratio on the undrained behaviour of granular materials. *Adv. Powder Technol.* **2022**, *33*, 103507. [CrossRef]
28. Liu, B.H.; Kong, L.W.; Sun, Z.L.; Zhou, Z.H. Undrained dynamic response of naturally high-strength sensitive clay to bidirectional cyclic loadings under the plane strain condition. *Soil Dyn. Earthq. Eng.* **2022**, *163*, 107517. [CrossRef]
29. Huang, K.; Ma, Q.Y.; Ma, D.D.; Yao, Z.M. Strength and deformation properties of frozen sand under a true triaxial stress condition. *Soils Found.* **2022**, *62*, 101089. [CrossRef]
30. Shao, S.; Shao, S.J.; Wang, Q. Strength Criteria Based on Shear Failure Planes and Test Verification on Loess. *Geotech. Test. J.* **2019**, *42*, 347–364. [CrossRef]
31. Liu, J.S.; Jing, H.W.; Meng, B.; Wang, L.G.; Yang, J.J.; You, Y.W.; Zhang, S.J. Fractional-order creep model for soft clay under true triaxial stress conditions. *Arab. J. Geosci.* **2020**, *13*, 834. [CrossRef]
32. Wang, D.; Liu, E.L.; Zhang, D.; Yue, P.; Wang, P.; Kang, J.; Yu, Q.H. An elasto-plastic constitutive model for frozen soil subjected to cyclic loading. *Cold Reg. Sci. Technol.* **2021**, *189*, 103341. [CrossRef]
33. Yamada, S.; Sakai, T.; Nakano, M.; Noda, T. Method to Introduce the Cementation Effect into Existing Elastoplastic Constitutive Models for Soils. *J. Geotech. Geoenviron. Eng.* **2022**, *148*, 04022013. [CrossRef]
34. Zheng, Y.; Fan, Z.; Tan, Q.; Xu, Y. Construction of elastic viscoplastic constitutive model and settlement control of over-consolidated soil using finite element software ABAQUS. *Arab. J. Geosci.* **2021**, *14*, 257. [CrossRef]
35. Tachibana, S.; Matsumoto, M.; Iizuka, A. Practical method to estimate parameters of elasto-plastic constitutive model for unsaturated soils from compaction curve. *Soils Found.* **2020**, *60*, 1287–1298. [CrossRef]
36. Zhao, Y.H.; Lai, Y.M.; Pei, W.S.; Yu, F. An anisotropic bounding surface elastoplastic constitutive model for frozen sulfate saline silty clay under cyclic loading. *Int. J. Plast.* **2020**, *129*, 102668. [CrossRef]
37. Zhang, D.; Liu, E.L.; Yu, D. A micromechanics-based elastoplastic constitutive model for frozen sands based on homogenization theory. *Int. J. Damage Mech.* **2020**, *29*, 689–714. [CrossRef]
38. Peng, F.L.; Siddiquee, M.S.A.; Tatsuoka, F.; Yasin, S.J.M.; Tanaka, T. Strain Energy-Based Elasto-Viscoplastic Constitutive Modelling of Sand for Numerical Simulation. *Soils Found.* **2009**, *49*, 611–629. [CrossRef]

39. Mazzucco, G.; Pomaro, B.; Salomoni, V.A.; Majorana, C.E. Apex control within an elasto-plastic constitutive model for confined concretes. *Math. Comput. Simul.* **2019**, *162*, 221–232. [CrossRef]
40. Sternik, K. Elasto-plastic Constitutive Model for Overconsolidated Clays. *Int. J. Civ. Eng.* **2017**, *15*, 431–440. [CrossRef]